A non-conducting role of the $Ca_v1.4$ Ca^{2+} channel drives homeostatic plasticity at the cone photoreceptor synapse

J. Wesley Maddox[1,6], Gregory J. Ordemann[1,6], Juan de la Rosa Vázquez [1], Angie Huang,[1] Christof Gault,[1] Serena R. Wisner[2,3], Kate Randall[1], Daiki Futagi[4], Nihal A. Salem[1], R. Dayne Mayfield[1], Boris V. Zemelman[1], Steven H. DeVries[4], Mrinalini Hoon[2,5] and Amy Lee[1*]

[1]Dept of Neuroscience, University of Texas-Austin, Austin, TX 78712, USA

[2]Dept. of Ophthalmology and Visual Sciences, University of Wisconsin- Madison, Madison, WI, 53706, USA

[3]Neuroscience Training Program, University of Wisconsin-Madison, Madison WI 53706 USA

[4]Dept. of Ophthalmology, Northwestern University Feinberg School of Medicine, Chicago, IL, 60611, USA

[5] McPherson Eye Research Institute, Madison WI 53706 USA

[6]These authors contributed equally

[*]Corresponding author, email: amy.lee1@austin.utexas.edu

ABSTRACT

In congenital stationary night blindness type 2 (CSNB2)—a disorder involving the $Ca_v1.4$ (L-type) Ca^{2+} channel—visual impairment is mild considering that $Ca_v1.4$ mediates synaptic release from rod and cone photoreceptors. Here, we addressed this conundrum using a $Ca_v1.4$ knockout (KO) mouse and a knock-in (G369i KI) mouse expressing a non-conducting $Ca_v1.4$. Surprisingly, Ca_v3 (T-type) Ca^{2+} currents were detected in cones of G369i KI mice and $Ca_v1.4$ KO mice but not in cones of wild-type mouse, ground squirrel, and macaque retina. Whereas $Ca_v1.4$ KO mice are blind, G369i KI mice exhibit normal photopic (i.e., cone-mediated) visual behavior. Cone synapses, which fail to form in $Ca_v1.4$ KO mice, are present, albeit enlarged, and with some errors in postsynaptic wiring in G369i KI mice. While $Ca_v1.4$ KO mice lack evidence of cone synaptic responses, electrophysiological recordings in G369i KI mice revealed nominal transmission from cones to horizontal cells and bipolar cells. In CSNB2, we propose that Ca_v3 channels maintain cone synaptic output provided that the nonconducting role of $Ca_v1.4$ in cone synaptogenesis remains intact. Our findings reveal an unexpected form of homeostatic plasticity that relies on a non-canonical role of an ion channel.

KEYWORDS: photoreceptor, Ca^{2+} channel, ribbon synapse, retina, synaptogenesis

INTRODUCTION

At the first synapse in the visual pathway, graded electrical signals produced in rod and cone photoreceptors gate the release of glutamate onto postsynaptic neurons. Photoreceptor synapses are specialized with a ribbon organelle, which helps prime synaptic vesicles, [1, 2] and postsynaptic neurites of horizontal and bipolar cells that invaginate deep within the terminal [3]. A variety of proteins interact with the ribbon and synaptic vesicles near release sites (*i.e.,* active zones) [4]. The importance of these proteins for vision is illustrated by the numerous inherited retinal diseases linked to mutations in their encoding genes [5].

52 One such gene is *CACNA1F*, which encodes the voltage-gated Ca^{2+} (Ca_v) channel
53 expressed in retinal photoreceptors, $Ca_v1.4$ [6-8]. Among the sub-family of Ca_v1 L-type channels,
54 $Ca_v1.4$ exhibits unusually slow inactivation that is well-matched for supporting the tonic, Ca^{2+}-
55 dependent release of glutamate from photoreceptor synaptic terminals in darkness [9, 10]. More than
56 200 mutations in *CACNA1F* cause vision disorders including congenital stationary night blindness
57 type 2 (CSNB2) [11, 12]. These mutations are broadly categorized as producing a gain of function or
58 loss of function in $Ca_v1.4$ [13]. How these mutations in *CACNA1F* lead to the variable clinical
59 phenotypes of CSNB2 is largely unknown. Symptoms may include strabismus, low visual acuity,
60 and in many cases, night blindness [14, 15]. The latter suggests a primary defect in rod pathways,
61 which is surprising given that $Ca_v1.4$ knockout (KO) mice are completely blind and lack any
62 evidence of either rod or cone synaptic responses [6, 7, 16]. A major caveat is that rod and cone
63 synapses do not form in $Ca_v1.4$ KO mice [7, 16-18]. Thus, $Ca_v1.4$ KO mice are not suitable for studies
64 of how *CACNA1F* mutations differentially affect rod and cone pathways or for efforts to uncover
65 how the biophysical properties of $Ca_v1.4$ shape photoreceptor synaptic release properties.
66 Here, we overcome this hurdle with a knock-in mouse strain (G369i KI) expressing a non-
67 conducting mutant form of $Ca_v1.4$ [19]. We show that, although greatly impaired, cone synapses
68 and downstream signaling through cone pathways can support photopic visual function in G369i
69 KI mice. This novel mechanism requires the ability of the $Ca_v1.4$ protein, independent of its Ca^{2+}
70 conductance, to nucleate the assembly of cone ribbon synapses and involves an aberrant Ca_v3
71 (T-type) conductance that appears when $Ca_v1.4$ Ca^{2+} signals are compromised.
72
73 **RESULTS**
74 *Cone pedicles and ribbons are present in G369i KI mice but not in $Ca_v1.4$ KO mice*
75 The G369i mutation results in an insertion of a glycine residue in a transmembrane
76 domain, which prevents Ca^{2+} permeation through $Ca_v1.4$[19]. The presence of rod synapses in
77 G369i KI mice but not $Ca_v1.4$ KO mice indicates that the $Ca_v1.4$ protein and not its Ca^{2+}

conductance is required for rod synapse assembly[19]. To test if this is also true for cones, we performed immunofluorescence and confocal analyses using antibodies against cone arrestin (CAR) and CtBP2 to label cone terminals (i.e., pedicles) and ribbons, respectively (Fig. 1). In $Ca_v1.4$ KO mouse retinas, cone pedicles were shrunken and retracted into the outer nuclear layer (ONL, Fig. 1a) with little evidence of elongated ribbons (Fig. 1b). In contrast, cone pedicles in G369i KI mice were normally localized in the outer plexiform layer (OPL, Fig. 1a) and were populated by multiple ribbons that were associated with labeling for $Ca_v1.4$ (Fig. 1b). Some abnormalities were apparent in G369i KI cone pedicles, such as extremely elongated ribbons and telodendria extending towards the inner nuclear layer (Fig.1b). These results indicate that $Ca_v1.4$ Ca^{2+} signals are dispensable for the integrity of ribbons and the pedicle but are necessary for their overall refinement.

Ca_v3 channel activity is present in cones of G369i KI and $Ca_v1.4$ KO mice but not WT mice, ground squirrel, or macaque retina

A prevailing yet unsupported hypothesis regarding the relatively mild visual phenotypes in CSNB2 is that additional Ca_v subtypes may compensate for $Ca_v1.4$ loss-of-function in cones. If so, then Ca^{2+} currents (I_{Ca}) mediated by these subtypes should be evident in cones of $Ca_v1.4$ KO and G369i KI mice. To test this, we performed patch clamp recordings of cones in retinal slices of adult WT, G369i KI, and $Ca_v1.4$ KO mice under conditions designed to isolate I_{Ca}. During voltage ramps in WT cones, I_{Ca} activated around -50 mV and peaked near -20 mV, consistent with the properties of $Ca_v1.4$ (Fig. 2a-d). While not observed in rods of G369i KI or $Ca_v1.4$ KO mice[19], a small-amplitude I_{Ca} that activated around -60 mV and peaked near -35 mV was detected in cones of these mice (Fig.2a-d). To uncover this low voltage-activated I_{Ca}, we used a faster voltage ramp (0.5 mV/ms) than in the previous study of G369i KI rods (~0.15 mV/ms)[19]. With this faster voltage ramp, I_{Ca} was not apparent in G369i KI rods (Supp.Fig.S1). Therefore, the aberrant I_{Ca} is an adaptation to $Ca_v1.4$ loss-of-function in cones but not rods.

104 We next used step depolarizations to identify the type of Ca_v channel underlying I_{Ca} in
105 G369i KI and $Ca_v1.4$ KO cones. Analysis of current-voltage (I-V) and conductance-voltage (G-V)
106 relationships revealed a significant, hyperpolarizing shift (~10 mV) in the voltage of half maximal
107 activation (V_h) in G369i KI cones (Fig.2c,d; Table 1). I_{Ca} in G369i KI cones was not sustained as
108 in WT cones but inactivated rapidly during 500-ms step depolarizations (Fig. 2e). For G369i KI
109 cones, overlay of the conductance-voltage (Fig. 2d) and inactivation curves revealed a sizeable
110 window current (Fig. 2f). These features of I_{Ca} in G369i KI and $Ca_v1.4$ KO cones resembled those
111 of Ca_v3 T-type channels rather than $Ca_v1.4$[20].

112 In a previous study, a Ca_v3-like current was detected in patch clamp recordings of cone
113 pedicles in WT mouse cones[21]. However, in recordings of WT mouse cone somas, we did not
114 observe a low-voltage activated component in the I-V or G-V curves that would be indicative of a
115 Ca_v3 subtype (Fig.2c,d). To further test for a Ca_v3 contribution to I_{Ca} in WT mouse cones, we used
116 a double pulse voltage protocol where I_{Ca} was evoked before (P1) and after (P2) a 500-ms step
117 to -60 mV (Fig.2g). With this protocol, the inactivation of Ca_v3 channels by the -60 mV step should
118 lead to a reduction in the amplitude of the P2 vs the P1 current. While such a reduction was clearly
119 evident in cones of G369i KI mice (i.e., P2/P1 < 1), there was no significant difference in the P2
120 and P1 currents in cones of WT mice (Fig.2g-i).

121 We also used antagonists selective for Ca_v1 and Ca_v3 channels (isradipine and ML 218,
122 respectively). As expected, I_{Ca} in WT cones was significantly but incompletely suppressed by
123 isradipine (Fig. 3a,b). The V_h of the I-V was similar before (-36.5 $\pm$ 0.8 mV) and after (-38.3 $\pm$ 1.8
124 mV) perfusion of isradipine ($t(3,4)=0.90$, $p = 0.43$ by paired t-test), suggesting that the residual I_{Ca}
125 after exposure to isradipine arose from unblocked $Ca_v1.4$ rather than Ca_v3 channels. While ML
126 218 modestly inhibited I_{Ca} in some WT cones, the effect was not statistically significant (Fig. 3c,d)
127 and could be attributed to weak activity on $Ca_v1.4$. In transfected HEK293T cells, ML 218 modestly
128 inhibited I_{Ca} and caused a negative shift in the V_h for $Ca_v1.4$, in contrast to its strong inhibition of

129 $Ca_v3.2$ (Supp.Fig. S2). Like its effects on $Ca_v3.2$, ML 218 nearly abolished I_{Ca} in cones of G369i
130 KI mice whereas isradipine had little effect (Fig. 3a-d).

131 Finally, we recorded from ground squirrel and macaque cones, where the large amplitude
132 of I_{Ca} facilitates pharmacological and biophysical analyses. Consistent with its actions on $Ca_v1.4$
133 in WT mouse cones (Fig. 3b) and transfected HEK293T cells (Supp.Fig. S2), ML 218 caused an
134 insignificant inhibition of peak I_{Ca} (-7.0 ± 20.8%, n = 6 cones) as well as a negative shift in the
135 voltage-dependence of activation in ground squirrel cones ($\Delta V_{1/2}$ = -1.16 ± 0.94 mV, n = 6, mean
136 ± SD, p = 0.029, t-test; Fig. 4a,b). By contrast, application of isradipine dramatically suppressed
137 I_{Ca} in cones in various regions of the ground squirrel retina (Fig. 4c,d). Subsequent application of
138 ML 218 did not reveal a Ca_v3-like current: the I-V and G-V of the isradipine + ML 218-sensitive
139 current were shifted in the positive rather than the negative direction relative to the isradipine-
140 sensitive current (Fig.4c-g). This result is consistent with the time- and voltage-dependent block
141 of Ca_v1 channels by dihydropyridine antagonists such as isradipine [22]. As a positive control, we
142 confirmed that ML 218 blocked a prominent Ca_v3-type current in ground squirrel type 3a OFF
143 cone bipolar cells (Fig.4h,i). In recordings of macaque cone pedicles, we compared the properties
144 of I_{Ca} using a holding voltage of -90 mV or -50 mV, the latter of which should inactivate Ca_v3
145 channels (Fig.5a). There was no difference in the I-V or G-V relationships obtained at these
146 holding voltages (Fig.5b-e). As in WT mouse cones (Fig.2g-i), there was also no difference in I_{Ca}
147 recorded before and after an inactivating pulse to -60 mV (Fig.5f,g). We conclude that Ca_v3
148 channels do not normally contribute to I_{Ca} in cones of WT mice, ground squirrel, and macaque.

149 To test whether the appearance of the Ca_v3-mediated I_{Ca} in G369i KI cones could result
150 from an increase in the expression of a specific Ca_v3 subtype (*i.e.,* $Ca_v3.1$, $Ca_v3.2$, or $Ca_v3.3$), we
151 initially tried labeling with commercially available antibodies against $Ca_v3.2$. However, the data
152 were unreliable since these antibodies produced a similar labeling pattern in $Ca_v3.2$ KO retinal
153 tissue (data not shown). As an alternative, we performed single cell RNA sequencing on cells
154 isolated from the retina of WT and G369i KI mice (Supp. Fig.S3). We sequenced 28,782 cells

155 and, with unsupervised clustering at resolution=0.5, we grouped the cells into 20 clusters. Clusters
156 8 and 16 were identified as cones based on the expression of cone marker genes (e.g., Opn1sw,
157 Opn1mw, Arr3, Gnat2). Consistent with previous studies[21, 23], *Cacna1h* encoding the $Ca_v3.2$
158 subtype was the major Ca_v3 transcript expressed in WT mouse cones. There was no significant
159 difference in *Cacna1h* expression between WT and G369i KI cones according to this analysis
160 (Supp. Fig.S3). Thus, the enhanced activity of Ca_v3 channels in cones of G369i KI mice results
161 from a mechanism other than increased transcription of *Cacna1h*.
162
163 *Cone synapses are enlarged with some errors in postsynaptic wiring in G369i KI mice*
164 The replacement of $Ca_v1.4$ with Ca_v3 as the primary conduit for Ca^{2+} influx in G369i KI
165 cones allowed us to dissect the importance of $Ca_v1.4$ Ca^{2+} signals for the molecular and structural
166 organization of the cone synapse. To this end, we first analyzed WT and G369i KI cone synapses
167 by immunofluorescence and confocal microscopy. Presynaptic proteins such as bassoon and
168 members of the postsynaptic signaling complex in depolarizing (ON) cone bipolar cells (GPR179,
169 mGluR6, and TRPM1[24]) were enriched near cone ribbons in G369i KI mice as in WT mice (Fig.
170 6a). Compared to WT mice, the labeled structures in G369i KI mice occupied a larger volume
171 (Fig. 6b,c) but were of lower intensity (Fig. 6d), suggesting an increase in the spread rather than
172 in the levels of synaptic proteins. Unlike in WT mice, the volume of presynaptic and postsynaptic
173 proteins increased linearly with the volume of the pedicle in G369i KI mice (Fig. 6e-i). These
174 results show that the molecular determinants of the cone synapse can assemble in G369i KI mice
175 but change in their sub-synaptic distribution in ways that correlate with the expansion of the cone
176 pedicle.
177 The cone synapse is structurally complex, with the dendritic tips of two horizontal cells
178 and an intervening ON cone bipolar cell invaginating deeply into the pedicle near the ribbon [3]. To
179 test how the switch in Ca_v subtypes might affect this arrangement of postsynaptic partners, we
180 generated 3D reconstructions of cone synapses by serial block-face scanning electron

181 microscopy (SBFSEM; Fig. 7). As with the enlarged synaptic contacts (Fig. 6), structural
182 modifications in G369i KI pedicles were evident. Compared to WT, ribbons in G369i KI pedicles
183 appeared disorganized and were often parallel rather than perpendicular to the presynaptic
184 membrane (Fig.7a-c). Consistent with our confocal analyses (Fig.1), G369i KI cone pedicles
185 extended telodendria in multiple directions rather than just apically (Fig. 7a). In addition, a slightly
186 larger fraction of synaptic sites in the G369i KI pedicle (35% vs 14% in WT) formed incorrect
187 postsynaptic partnerships including with glia (Fig.7b-d'; Table 2). Nevertheless, the number of
188 ribbons is normal in G369i KI cones and about half of the ribbons make invaginating contacts with
189 the appropriate cell types (*i.e.,* both horizontal cells and cone bipolar cells; Table 2). On average,
190 there were more vesicles associated with ribbons in cones of G369i KI mice (245 per ribbon) than
191 of WT mice (178 per ribbon; Table 2), but the difference did not reach statistical significance.
192 Together with our immunofluorescence data, these results indicate that cone synapses undergo
193 relatively subtle morphological changes in G369i KI mice, perhaps in response to the loss of
194 $Ca_v1.4$ Ca^{2+} signals.
195
196 *Postsynaptic responses to light are present in horizontal cells of G369i KI mice but not $Ca_v1.4$ KO*
197 *mice*
198 Compared to $Ca_v1.4$ KO mice, the relative preservation of cone synapses in G369i KI mice
199 allowed the unique opportunity to test whether a Ca_v subtype other than $Ca_v1.4$ could support
200 synaptic release. To this end, we analyzed synaptic transmission between cones and horizontal
201 cells (HCs). In darkness, glutamate released from cones depolarizes horizontal cells via activation
202 of α-amino-3-hydroxy-5-methyl-4-isoxazolepropionic (AMPA)/kainate receptors[25, 26]. The resulting
203 excitatory postsynaptic current (EPSC) undergoes a decline in response to light stimuli that
204 hyperpolarize cones[27]. In WT HCs, a 1-s light flash (λ=410 nm) inhibited the standing EPSC,
205 which is reflected as an outward (hyperpolarizing "ON") current (Fig. 8a). Upon termination of the
206 light, an inward (depolarizing "OFF") current signaled the resumption of the EPSC (Fig. 8a). Both

207 the ON and OFF responses in WT HCs increased with light intensity, reflecting the impact of
208 luminance on the presynaptic membrane potential of cones and the subsequent change in
209 glutamate release from their terminals (Fig. 8b).

210 Consistent with the lack of mature ribbons and abnormal cone pedicles (Fig.1), HC light
211 responses were negligible in $Ca_v1.4$ KO mice (Fig.8a,b). In contrast, the ON and OFF responses
212 were present in G369i KI HCs although significantly lower in amplitude than in WT HCs (Fig.
213 8a,b). As expected, the EPSC in darkness and the light responses were abolished by the
214 AMPA/kainate receptor antagonist, DNQX, in both WT and G369i KI HCs (Fig. 8c,d). In addition
215 to its smaller amplitude, the transient nature of the ON response in G369i KI HCs suggested
216 inadequate cessation of cone glutamate release by light (Fig.8b). Slow deactivation of Ca_v3
217 channels and/or their activation at negative voltages[20] could give rise to Ca^{2+} signals that support
218 release following light-induced hyperpolarization of G369i KI cones.

219 To test if the diminished HC light responses correlated with lower presynaptic Ca^{2+} signals
220 in G369i KI cones, we performed 2-photon imaging of cone pedicles filled with the Ca^{2+} indicator
221 Fluo3 and labeled with Alexa-568-conjugated peanut agglutinin. In WT cones, depolarization by
222 K^+ (50 mM) caused a sustained increase of Ca^{2+} ($\Delta F/F_0$ = 1.85 ± 0.1, n = 11 terminals) that was
223 significantly lower after the addition of isradipine ($\Delta F/F_0$ = 1.44 ± 0.07, p = 0.0015 by repeated
224 measures one-way ANOVA with Tukey's multiple comparison posthoc test; F[1.608, 16.08] =
225 55.17; p < 0.0001; Fig.9a,b). The Ca^{2+} signal remaining in the presence of isradipine could arise
226 from unblocked $Ca_v1.4$ channels and/or Ca^{2+} release from intracellular stores[28]. In G369i KI
227 cones, the peak amplitude of the K^+-evoked Ca^{2+} signal ($\Delta F/F_0$ = 1.07 ± 0.02, n = 14 terminals)
228 was significantly lower than in WT cones (t(23)=8.74, p < 0.0001 by unpaired t-test, n = 14
229 terminals). The decrease in the Ca^{2+} signal in the G369i KI cone pedicles during isradipine
230 exposure paralleled that during the depolarization (Fig.9a), suggesting it was not a consequence
231 of Ca_v1 blockade. The lower amplitude and more transient Ca^{2+} signals mediated by Ca_v3
232 channels may be cleared more rapidly in G369i KI cones as compared to prolonged $Ca_v1.4$-

233 initiated Ca^{2+} signals in WT cones. Taken together, our results suggest that Ca_v3 channels
234 nominally support Ca^{2+} signals and synaptic transmission in cones of G369i KI mice.
235
236 *Light responses of bipolar cells and visual behavior are present in G369i KI but not $Ca_v1.4$ KO*
237 *mice*
238 While HCs play important roles in lateral inhibition of photoreceptor output, the vertical
239 dissemination of visual information from cones to the inner retina is relayed by glutamate to ON
240 and OFF cone bipolar cells (CBCs) which express mGluR6 and AMPA/kainate receptors,
241 respectively. To test for the existence of cone to CBC transmission in G369i KI mice, we recorded
242 electroretinograms (ERGs) under light-adapted conditions using $Ca_v1.4$ KO mice as a negative
243 control (Fig. 10a-d). In these recordings, the light-induced response of photoreceptors and the
244 postsynaptic response of ON CBCs corresponds to the a- and b-waves, respectively. Unlike in
245 $Ca_v1.4$ KO mice, the a-waves of G369i KI mice resembled those in WT mice, which indicates that
246 cones do not degenerate in this mouse strain (Fig. 10a,b). While greatly reduced in amplitude,
247 the b-wave was measurable in G369i KI mice and significantly larger than in $Ca_v1.4$ KO mice at
248 the highest light intensities ($F(14,104)=41$, $p<0.0001$, post-hoc Tukey's $p=0.0038$ at 2.3 log
249 $cd{\cdot}s/m^2$; Fig. 10a,b). We also recorded flicker ERGs using 10 Hz light stimuli that can isolate cone
250 pathways involving both ON and OFF CBCs[29, 30]. In WT mice, flicker responses exhibited two
251 peaks, one at a lower irradiance (-2 log $cd{\cdot}s/m^2$) and one at higher irradiance (0.5 log $cd{\cdot}s/m^2$;
252 Fig.10c,d). The peak at the lower irradiance is attributed to responses in both rod and cone
253 pathways, and the peak at higher irradiance is attributed to responses exclusively in cone
254 pathways[29, 30]. Flicker responses in G369i KI mice showed a similar non-monotonic relation as in
255 WT mice but were significantly lower in amplitude ($F(26,143)=51.18$, $p<0.0001$, post-hoc Tukey's
256 $p=0.0237$ at 2.5 log $cd{\cdot}s/m^2$; Fig.10c,d). The inverted flicker responses at higher illuminations in
257 G369i KI mice were absent in $Ca_v1.4$ KO mice and may result from the hyperpolarizing
258 contribution of cone-to-OFF CBC transmission (Fig.10c).

259 To test whether the cone synaptic responses in G369i KI mice enable vision-guided
260 behavior, we used a swim test that assesses the ability of mice to identify a visible platform[31].
261 Under scotopic (dark) conditions, G369i KI and $Ca_v1.4$ KO mice took significantly longer to find
262 the platform compared to WT mice (Fig. 10e,f). These results are consistent with flicker response
263 assays (Fig.10c,d) as well as the absence of I_{Ca} in rods and rod-to-rod bipolar cell synaptic
264 transmission in G369i KI mice[19]. Under photopic (light) conditions, G369i KI mice but not $Ca_v1.4$
265 KO mice performed as well as WT mice (Fig. 10e,f). Thus, G369i KI mice have enough visual
266 function under photopic conditions to quickly find the platform. Collectively, our results suggest
267 that Ca_v3 channels can support cone synaptic responses that are sufficient for visual behavior in
268 G369i KI but not $Ca_v1.4$ KO mice.
269
270 **DISCUSSION**
271 The nervous system has remarkable abilities to adapt to pathological perturbations in
272 neuronal activity. In the retina, ablation or degeneration of photoreceptors triggers various
273 postsynaptic mechanisms that maintain some level of visual function in rod or cone pathways.
274 These include remodeling of bipolar cell dendrites and their synapses[32-34] as well as changes in
275 the sensitivity of bipolar cells to photoreceptor input and inhibitory modulation[34, 35]. To our
276 knowledge, this study provides the first evidence for a presynaptic form of homeostatic plasticity
277 that originates within photoreceptors. Using $Ca_v1.4$ KO and G369i KI mice, we identify the
278 upregulation of a Ca_v3 conductance as a common response to $Ca_v1.4$ loss-of-function in cones.
279 However, Ca_v3 channels can only compensate for $Ca_v1.4$ loss-of-function if the basic aspects of
280 cone synapse structure are maintained through expression of the G369i mutant channel. Thus,
281 our results also highlight a crucial, non-conducting role for the $Ca_v1.4$ protein that allows cone
282 synapses to function in the absence of $Ca_v1.4$ Ca^{2+} signals.
283
284 *A non-canonical role for $Ca_v1.4$ in regulating cone synapse assembly*

285 As shown for rod synapses[19], ribbons and other components of the pre- and post-synaptic
286 complex assemble at cone synapses in G369i KI mice (Figs. 1,6,7). Ca_v3 Ca^{2+} signals are
287 dispensable for this process since their presence in $Ca_v1.4$ KO cones is not accompanied by any
288 semblance of ribbon synapses (Fig.1b). An intimate relationship between $Ca_v1.4$ and ribbons is
289 supported by the colocalization of $Ca_v1.4$ and puncta resembling ribbon precursor spheres in the
290 developing OPL[7]. $Ca_v1.4$ interacts directly or indirectly with a variety of ribbon synapse associated
291 proteins including RIM [36], CAST/ERC2 [37], bassoon[38], unc119[39-41], and a major component of the
292 ribbon, RIBEYE[42]. $Ca_v1.4$ could pioneer sites of ribbon assembly perhaps by serving as a docking
293 or nucleation site for the active zone. At the same time, ribbon-associated proteins help cluster
294 $Ca_v1.4$ near ribbons since knockout of these proteins in mice leads to fewer presynaptic $Ca_v1.4$
295 channels and in some cases shortened ribbons[43]. Regardless of the mechanism, our findings
296 show that the formation of photoreceptor synaptic complexes does not require Ca^{2+} influx through
297 $Ca_v1.4$ channels.
298
299 *Functional Ca_v3 channels are present in cones in the absence of $Ca_v1.4$ Ca^{2+} signals*
300 Our drop-seq analysis aligns with previous studies indicating that *Cacna1h* is expressed
301 at extremely low levels compared to *Cacna1f* in WT mouse cones (Supp.Fig.S3)[23, 44]. However,
302 in contrast to recordings of WT mouse cone pedicles in a previous study[21], we found no evidence
303 for Ca_v3-mediated currents in somatic recordings of cones in WT mice (Figs.2,3). We do not feel
304 the discrepancy results from the different recording configurations given the electrically compact
305 nature of cones. Moreover, recordings from macaque cone pedicles and from the ellipsoids of
306 cylindrically-shaped ground squirrel cones also did not reveal a Ca_v3-mediated current (Figs.4,5).
307 We acknowledge that there are caveats of the pharmacological approach used in our study as
308 well as the previous work[21]. For example, dihydropyridine antagonists such as isradipine have
309 relatively low affinity for some Ca_v1 subtypes, including $Ca_v1.4$[22, 45] and have strongly voltage-
310 dependent blocking properties. At a holding voltage of -90 mV, isradipine at 1 μM causes only

311 ~80% inhibition of $Ca_v1.4$ with greater block at depolarized voltages[22], which agrees with our
312 recordings of cones in WT mice (Fig.3a) and ground squirrels (Fig.4b-e). Moreover, in the low
313 micromolar range, Ca_v3 blockers such as Z944 [46] and ML 218 (Supp.Fig. S2) have nonspecific
314 effects on Ca_v1 current amplitude and activation voltage. Thus, Ca_v channels mediating a I_{Ca} that
315 is suppressed by Ca_v3 blockers and spared by dihydropyridines at negative voltages may be
316 mistakenly categorized as Ca_v3 subtypes. In our experiments, the biophysical properties of the
317 isradipine-sensitive I_{Ca} in cones of WT mice and ground squirrels resembled only those of Ca_v1,
318 whereas those of the ML 218-sensitive I_{Ca} in cones of G369i KI mice resembled only those of
319 Ca_v3. Therefore, we favor the interpretation that Ca_v3 contributes to I_{Ca} in mouse cones only upon
320 silencing of $Ca_v1.4$ either by KO of the corresponding protein or by silencing its conductance.
321 Since *Cacna1h* expression was similar in WT and G369i KI cones (Supp.Fig.S3), what
322 causes the increased Ca_v3 channel activity in the latter? Among the Ca_v3 subtypes, $Ca_v3.2$ is
323 uniquely sensitive to post-translational modifications that facilitate the opening of the channel
324 and/or its cell surface trafficking[47]. For example, $Ca_v3.2$ interacts with the deubiquitinating enzyme
325 USP5 which enhances levels of $Ca_v3.2$ protein levels by suppressing its proteasomal
326 degradation[48]. In addition, $Ca_v3.2$ is phosphorylated by calmodulin-dependent kinase II[49] and
327 cyclin-dependent kinase 5[50], which enhances channel activation and current density, respectively.
328 Further interrogation of our drop-seq dataset could illuminate novel $Ca_v3.2$-regulatory pathways
329 that are modified in G369i KI cones.
330
331 *Consequences of $Ca_v1.4$ loss of function and relevance for CSNB2*
332 Despite having the same complement of proteins as in WT mice, cone synapses in G369i
333 KI mice were enlarged and made errors in postsynaptic partner selection (Figs.6,7). While I-V
334 curves indicate similar peak I_{Ca} amplitudes in cones of WT and G369i KI mice near the membrane
335 potential of cones in darkness (-45 to -50 mV[51], Fig.2a,c), the strong inactivation of Ca_v3 channels
336 and/or reduced Ca^{2+} release from intracellular stores likely account for the greatly diminished Ca^{2+}

signals in G369i KI pedicles (Fig.9). Paradoxically, reductions in presynaptic Ca^{2+} in rod photoreceptors correlated with illumination-dependent shrinkage of ribbons *in vivo* and *in vitro*[2, 52, 53]. However, ribbon synapse size increases with low presynaptic Ca^{2+} in zebrafish sensory hair cells[54]. The mechanism involves decreased mitochondrial Ca^{2+} uptake and increase in the redox state of nicotinamide adenine dinucleotide (NAD^+/NADH ratio) [55]. Ca_v3 Ca^{2+} signals may decay too quickly in G369i KI cones (Fig.9) to enable mitochondrial Ca^{2+} uptake or other mechanisms that trim ribbons.

An intriguing result was the linear increase in ribbon synapse size with pedicle volume in G369i KI but not in WT mice (Fig. 6e-i), which could represent a form of homeostatic synaptic scaling as has been demonstrated at the neuromuscular junction[56, 57]. Similarly, the presence of some non-invaginating contacts with incorrect partner pairings in G369i KI mice (Fig.7, Table 2) could be an attempt to increase synaptic connectivity to compensate for weakened synaptic output. Consistent with this possibility, diminished presynaptic Ca^{2+} signals and non-invaginating cone synapses also characterize the retina of mice lacking the extracellular $\alpha_2\delta$–4 subunit of $Ca_v1.4$[58]. The cone synapses of G369i KI mice and $\alpha_2\delta$–4 KO mice are clearly functional given that photopic visual behavior is preserved in both mouse strains (Fig.10e,f)[58] and, in the case of G369i KI mice, HCs exhibit EPSCs whose amplitude decreases with light and AMPA/kainate receptor blockade (Fig.8). Defects in cone synaptic transmission that correlate with aberrant cone synapse morphology and connectivity also typify a mouse strain with a gain-of function mutation in $Ca_v1.4$ linked to CSNB2[59, 60]. Thus, balanced presynaptic Ca^{2+} signals may be needed to encode the correct post-synaptic wiring and structure of the cone synapse.

In addition to structural abnormalities in cone synapses, the inability of Ca_v3 channels to support sustained presynaptic Ca^{2+} entry likely contributed to the impaired light responses in HCs and CBCs in G369i KI mice (Figs.8,10). Due to their slow activation and strong inactivation [61], Ca_v3 channels are not expected to fuel the Ca^{2+} nanodomains that support fast and sustained

362 components of release, both of which occur only at ribbon sites in cones[1 62]. Ca_v3 channels may
363 also be located further from the ribbon than $Ca_v1.4$, thus lowering the efficiency of coupling to
364 exocytosis. Regardless of the features that differentiate the contributions of Ca_v3 and $Ca_v1.4$ to
365 cone synaptic release, our findings provide further support for the widely held view that Ca_v1
366 channels are well-suited to support transmission at ribbon-type synapses.

367 Based on extremely heterogeneous clinical presentations, CSNB2 manifests as a
368 spectrum of visual disorders that originate from various mutations in *CACNA1F* [14, 63]. Even though
369 some CSNB2 mutant $Ca_v1.4$ channels may traffic normally to the plasma membrane, many of
370 these mutations are expected to produce non-functional, non-conducting $Ca_v1.4$ channels[64, 65].
371 Yet, the visual phenotypes of CSNB2 patients are not as severe as the complete blindness in
372 $Ca_v1.4$ KO mice, which lack any $Ca_v1.4$ protein expression and exhibit no signs of visual behavior
373 (Fig.10e,f)[58]. Collectively, our results suggest that G369i KI mice accurately model $Ca_v1.4$
374 channelopathies in CSNB2 patients that are characterized by a greater impairment in rod than in
375 cone pathways. This interpretation is supported by our findings that G369i KI mice exhibit
376 horizontal cell responses to bright but not dim illumination (Fig. 8), ERG responses under
377 conditions of light adaptation (Fig.10a-d) but not dark-adaptation [19], and visual behavior under
378 photopic but not scotopic conditions (Fig. 10e,f). Together with the enlargement of synaptic sites,
379 modest levels of synaptic release from cones of G369i KI mice may support nominal transmission
380 of visual information through cone pathways. G369i KI mice could also exhibit homeostatic
381 alterations in the inner retina, which are known to support visual function when photoreceptor
382 input is severely compromised [33-35]. Future studies of the retinal circuitry and visual behavior of
383 G369i KI mice could identify compensatory pathways that are recruited upon $Ca_v1.4$ loss-of-
384 function and how they might be targeted in novel therapies for CSNB2 and related disorders.
385
386
387 **ACKNOWLEDGEMENTS**

J.W.M., G.J.O., J.D.V., A.H., K.R., and A.L. were supported by NIH grants EY026817 (to A.L.), EY029953 (to J.W.M.), and unrestricted funds from the University of Texas-Austin (to A.L.); S.R.W. and M.H. were supported by NIH grant EY031677 (to M.H.), an unrestricted grant from RPB to UW Madison Dept. of Ophthalmology and a McPherson ERI professorship to M.H.; D.F. and S.H.D. were supported by NIH grants EY012141 and EY032506, an unrestricted grant from RPB to the Northwestern University Dept. of Ophthalmology, and an RPB International Travel Award. N.A.S. and R.D. Mayfield were supported by AA029955 (N.A.S) and AA0012404 and AA020926 (R.D.M.). The authors thank J. Sun for assistance with acquiring some of the electrophysiological data in Supp.Fig.S2, S. Knecht and R. Wong for assistance with serial EM image collection, E. Seidemann and B. Shukla for the generous donation and collection of macaque retinal tissue, respectively, and M. McCall and F. Vinberg for advice on ERGs.

AUTHOR CONTRIBUTIONS

Conceptualization, J.W.M., G.O., A.L.; Methodology, J.W.M., G.O., J.D.V., A.L., M.H., S.H.D., D.F., N.S., R.D.M; Investigation, J.W.M., G.O., J.D.V., A.H., C.G., K.R., S.R.W., S.H.D., D.F.; Writing—original draft, A.L.; Writing—review and editing, J.W.M., G.J.O., M.H., S.H.D., A.L.; N.S., R.D.M. Funding acquisition, J.W.M., M.H., S.H.D., A.L., R.D.M.

DECLARATION OF INTERESTS

The authors declare no competing interests.

Table 1. Comparison of parameters from electrophysiological recordings of cones.

	C_M (pF)	P-value	n	R_M (MΩ)	P-value	n
WT	4.88 (3.86, 5.01)	--	11	3.57 (2.81, 4.65)	--	11
G369i KI	4.08 (3.88, 4.34)	0.73[a]	9	5.06 (4.04, 8.24)	0.04[a]	9
$Ca_v1.4$ KO	3.31 (3.00, 3.76)	0.001[a], 0.04[b]	6	8.21 (7.26, 9.06)	0.001[a], 0.47[b]	6
G-V	V_h (mV)	P-value	n	k	P-value	n
WT	-37.54 (-38.91, -35.13	--	13	2.75 (2.47, 4.32)		13
G369i KI	-47.59 (-50.07, -46.72)	0.0001[a]	9	2.99 (2.68, 4.16)	0.99[a]	9
$Ca_v1.4$ KO	-44.98 (-50.15, -43.27)	0.085[a], 0.99[b]	3	4.33 (3.73, 5.22)	0.34[a], 0.49[b]	3
Steady state inactivation	V_h (mV)	P-value	n	k	P-value	n
WT	-49.06 (-57.95, -41.82)	--	8	-7.25 (-12.30, -4.97)	--	8
G369i KI	-59.40 (-62.73, -58.01)	0.01[a]	8	-3.81 (-5.23, -2.46)	0.12[a]	8
$Ca_v1.4$ KO	-56.62 (-61.65, -56.56)	0.88[a], 0.88[b]	3	-3.67 (-5.17, -1.19)	0.14[a], 0.99[b]	3
	Tau activation	P-value	n	Tau deactivation	P-value	n
WT	2.04 (1.26, 2.71)	--	11	0.88 (0.62. 2.09)	--	6
G369i KI	3.32 (2.99, 4.06)	0.001[a]	9	3.40 (2.62, 4.34)	0.004[a]	6

Values represent median (25th, 75th quartiles). V_h and k were determined from Boltzmann fits of the G-V and steady-state inactivation curves. Time constant (tau) for activation was obtained from exponential fit of the rising phase of I_{Ca} evoked by a 50-ms test pulse to a voltage near the peak of the I-V. Tau deactivation was determined from exponential fit of the decay of the tail current evoked by repolarization to -90 mV from +20 mV. C_M, membrane capacitance; R_M, input resistance. P-values were determined by Kruskal Wallis test. [a], relative to WT. [b], relative to G369i KI.

Table 2. Comparison of parameters for cone synapse organization

	WT		G369i KI	
	Cone 1	Cone 2	Cone 1	Cone 2
# of ribbons	12	8	8	6
Mean # synaptic vesicles per ribbon	137.75	218.25	224	267.5
Type of contact: % total (fraction of total)				
Invaginating	58.3 (7/12)	87.5 (7/8)	50 (4/8)	50 (3/6)
Non-invaginating	41.7 (5/12)	12.5 (1/8)	50 (4/8)	50 (3/6)
Partner composition: % total (fraction of total)				
HC/BC	83.3	87.5	50.0	66.7
HC only	8.3	12.5	25.0	33.3
BC only	8.3	0	12.5	0
Glia only	0	0	12.5	0

Results represent analysis of n = 2 pedicles reconstructed by serial block face scanning electron microscopy in images obtained from WT or G369i KI mice (N= 1 animal each). The first row of vesicles encircling and immediately apposed to the ribbon were quantified for all the z-planes of the ribbon. Sites were counted as 'invaginating' if postsynaptic partners were enveloped on all sides by the cone terminal for at least a couple of consecutive image planes.

FIGURE LEGENDS

Figure 1. Cone pedicles and the mutant $Ca_v1.4$ G369i channel are normally localized in the retina of G369i KI mice but not $Ca_v1.4$ KO mice. Confocal images of the outer nuclear layer (ONL) and outer plexiform layer (OPL) of retina from WT, G369i KI, and $Ca_v1.4$ KO mice that were labeled with antibodies against cone arrestin (CAR), CtBP2, and $Ca_v1.4$. ***a***, Inverted images of CAR labeling. Lower panels depict pedicles labeled by CAR antibodies (dotted outlines) and correspond to the boxed regions in the upper panels. Cone pedicles remain in the OPL of WT and G369i KI retina (arrows) but are misshapen and retracted into the ONL of the $Ca_V1.4$ KO retina (open arrowheads). Solid arrowheads indicate telodendria which extend only apically in WT retina but extend basally and laterally in G369i KI retina. ***b***, Deconvolved confocal images showing $Ca_V1.4$ labeling near cone ribbons in WT and G369i KI pedicles (arrows) and ribbon spheres

451 without $Ca_V1.4$ labeling in the $Ca_V1.4$ KO pedicle (arrowheads). Rod-associated CtBP2 and
452 $Ca_v1.4$ labeling was removed for clarity.
453
454 **Figure 2. A low-voltage activated I_{Ca} is present in cones of G369i KI and $Ca_V1.4$ KO but**
455 **absent in cones of WT mice. *a*,** Representative traces of I_{Ca} evoked by voltage ramps. ***b,*** I_{Ca}
456 traces from *a* normalized to their peak current amplitude to illustrate the hyperpolarizing shift in
457 the I-V from cones of G369i KI and $Ca_V1.4$ KO mice. ***c,d***, I-V (*c*) and G-V (*d*) relationships for I_{Ca}
458 evoked by 50 ms, +5 mV increments from a holding voltage of -90 mV. V_m, test voltage. WT, n =
459 13; G369i KI, n = 9; $Ca_V1.4$ KO, n = 3. ***e*,** Representative I_{Ca} traces and voltage protocol (bottom)
460 for steady-state inactivation. I_{Ca} was evoked by a conditioning pre-pulse from -90 mV to various
461 voltages for 500 ms followed by a test pulse to -30 mV for 50 ms. ***f***, Steady-state inactivation data
462 from cones as recorded in *e*. I/I_{max} represents the current amplitude of each -30-mV test pulse (I)
463 normalized to current amplitude of the -30-mV test pulse preceded by a -90 mV conditioning pre-
464 pulse (I_{max}) and was plotted against pre-pulse voltage. Shaded region indicates window current
465 for G369i KI cones. Line without symbols represents G-V curve for G369i KI cones replotted from
466 *d*. WT, n = 8; G369i KI, n = 8; $Ca_v1.4$ KO, n = 3. In graphs *c,d,* and *f,* smooth lines represent
467 Boltzmann fits, symbols and bars represent mean ± SEM, respectively. ***g,*** Representative I_{Ca}
468 traces from WT and G369i KI cones and voltage protocol (top). I_{Ca} was evoked by a step from -
469 100 mV to -30 mV before (P1) or after (P2) a 500 ms step to -60 mV. ***h,i,*** Graphs depicting peak
470 amplitude of I_{Ca} during P1 and P2 steps (*h*) and the ratio of the amplitudes of I_{Ca} evoked by P2
471 and P1 pulses (P2/P1; *i*) from cones recorded as in *g*. WT, n = 6; G369i KI, n = 6, *$p < 0.05$ by
472 paired t-test.
473
474 **Figure 3. Pharmacological characterization of I_{Ca} in cones of WT and G369i KI mice.**
475 ***a,*** Representative traces for I_{Ca} evoked by voltage ramps in cones of retinas from WT (top) and
476 G369i KI (bottom) mice before (baseline) and after exposure to isradipine (ISR, 1 μM). Middle

477 panel, WT I_{Ca} from voltage ramps in the top panel were normalized to their peak I_{Ca} to clarify the
478 similar properties of I_{Ca} before and after ISR exposure. ***b,*** Peak I_{Ca} before (-) and during (+) ISR
479 exposure from cones as recorded in *a*. WT, n = 4; G369i KI, n = 5; *p < 0.05 by paired t-test. ***c,***
480 Representative traces for I_{Ca} evoked by voltage ramps in cones of retinas from WT or G369i KI
481 mice before (baseline) and after exposure to ML 218 (5 μM). Middle panel, WT I_{Ca} from voltage
482 ramps in the top panel were normalized to their peak I_{Ca} to clarify the similar properties of I_{Ca}
483 before and after ML 218 exposure. ***d,*** Peak I_{Ca} before (-) and during (+) ML 218 exposure. WT, n
484 = 5; G369i KI, n = 5; *p < 0.05 by paired t-test.
485
486 **Figure 4. Pharmacological characterization of I_{Ca} in ground squirrel cones**. ***a,***
487 Representative traces corresponding to baseline-corrected I_{Ca} evoked by voltage ramps before
488 (baseline) and during application of ML 218. ***b,*** G-V relationship of I_{Ca} in *a*. ***c,*** Representative
489 traces corresponding to I_{Ca} evoked by voltage ramps in control (baseline) and in ISR (2 μM) alone
490 or in ISR+ML 218 (5 μM). ***d,*** Peak I_{Ca} from cones including the record from *c* before (-) and during
491 (+) ISR or ISR+ML 218 block. The changes during the addition of ML218 were small but significant
492 (sup., n = 7, ISR: p < 0.0001, ML218: p = 0.0047; mid., n = 5, ISR: p < 0.0001, ML218: p = 0.0001;
493 inf., n = 5, ISR: p = 0.0019, ML218: p = 0.0460; two-tailed t test) and were likely due to a further
494 non-specific, time-dependent reduction in the Ca_v1 current. ***e,*** I_{Ca} was evoked by steps from -85
495 mV to voltages between -65 and -5 mV in increments of +10 mV (protocol shown below the current
496 traces in *f*). Representative traces are shown in control, ISR, or ISR+ML 218. Current traces
497 during steps to -55 and -45 mV lacked both transient and ML 218-senstive components. Dashed
498 lines indicate zero current. ***f,*** Traces show the I_{Ca} sensitive to ISR (top) and ISR+ML218 (middle).
499 The I_{Ca} recorded in ISR was subtracted from the baseline I_{Ca} (top). I_{Ca} recorded in ISR+ML218 was
500 subtracted from I_{Ca} recorded in ISR (middle). ***g,*** *Top*, I-V relationship of peak and steady-state I_{Ca}
501 from *f*. *Bottom*, G-V relationship of the I_{Ca} blocked by ISR and ISR + ML218. Smooth lines
502 represent Boltzmann fits. Symbols and bars represent mean ± SEM (n = 4 cones). Due a negative

503 shift in the activation properties caused by ML 218 on a residual Ca_v1 current that is assumed to
504 remain at the end of the experiment, the G-V curve of the I_{Ca} isolated through subtraction by
505 applying ISR+ML 281 underwent a statistically insignificant shift to the right. Data presented in *e-*
506 *g* are from the same cone. ***h,*** Representative I_{Ca} traces from voltage ramps in an OFF cb3a bipolar
507 cell before and during the application of ML 218. $V_{1/2}$ was shifted to the right by 13.1 ± 4.3 mV (n
508 = 3 cb3a cells, mean ± SD) consistent with the block of a Ca_v3-like conductance. In cb3b OFF
509 bipolar cells, ML 218 produced only a slight leftward shift in an I_{Ca} that had a more depolarized
510 activation range, consistent with the exclusive expression a Ca_v1-type current ($\Delta V_{1/2}$ = -1.9 ± 0.4
511 mV, n = 3 cells; data not shown). ***i,*** Neurobiotin fill shows cb3a axon stratification and morphology
512 in retina labeled with antibodies against bassoon and choline acetyltransferase (CHAT) to label
513 the OFF and ON sublamina of the IPL.
514
515 **Figure 5. Characterization of I_{Ca} in patch clamp recordings of cone pedicles of macaque**
516 **retina.** ***a-c,*** Representative current traces (*a*) and corresponding I-V (*b*) and G-V (*c*)
517 relationships for I_{Ca} evoked by 200-ms steps from a holding voltage of -90 mV or -50 mV. n = 3
518 cones. ***d,e,*** $V_{1/2}$ (*d*) and slope factor (*e*) obtained from Boltzmann fit of data in *c*. p = 0.50 in *d*; p
519 = 0.25 in *e* by Wilcoxon matched pairs signed rank test. ***f,*** Voltage protocol (*top*) and
520 representative I_{Ca} traces (*bottom left*) from cones as recorded in Fig. 2g-i. Bottom right,
521 expanded view of the boxed region in the left traces. ***g,*** Peak I_{Ca} during P1 and P2 steps from
522 cones recorded as in *f*. n = 5 cones, p = 0.62 by Wilcoxon matched pairs signed rank test.
523
524 **Figure 6. Immunofluorescence characterization of cone synapses in WT and G369i KI mice.**
525 ***a***, Confocal images of the OPL of WT and G369i KI mice labeled with antibodies against cone
526 arrestin (CAR) and proteins that are presynaptic (CtBP2, bassoon) or postsynaptic (GPR179,
527 TRPM1, mGluR6). Every other panel shows high-magnification, deconvolved images of single

528 pedicles labeled with cone arrestin (rod spherule-associated signals were removed for clarity).
529 Arrows indicate ribbon synapses, which appear enlarged in the G369i KI pedicles. ***b***, Violin plot
530 representing volume of presynaptic protein labeling normalized to the volume of their respective
531 CAR-labeled pedicles (volume occupancy). ***c,*** Violin plot representing volume of postsynaptic
532 protein labeling normalized to the volume of their respective CAR-labeled pedicles. ***d,*** Violin plot
533 representing fluorescence intensity of postsynaptic proteins. For *b-d*, **p < 0.01, ***p < 0.001,
534 ****p < 0.0001, unpaired t-tests. ***e-i***, Dependence of synapse size on pedicle size. Volumes
535 corresponding to labeling of CtBP2 (*e*: p = 0.051, r = 0.4 for WT; p < 0.0001, r = 0.88 for G369i
536 KI), $Ca_V1.4$ (*f*: p = 0.8, r = 0.06 for WT; p = 0.002, r = 0.88 for G369i KI), bassoon (*g*: p = 0.1, r =
537 0.34 for WT; p < 0.0001, r = 0.75 for G369i KI), mGluR6 (*h*: p = 0.32, r = 0.35 for WT; p = 0.002,
538 r = 0.73 for G369i KI) and TRPM1 (*i*: p = 0.32, r = 0.35 for WT; p = 0.007, r = 0.66 for G369i KI)
539 are plotted against pedicle volume. Dashed and solid lines represent fits by linear regression for
540 WT and G369i KI, respectively.
541
542 **Figure 7. Three-dimensional reconstruction of cone synapses by SBFSEM.** Reconstructions
543 were made of WT and G369i KI pedicles (n = 2 each). ***a***, 3D renderings showing ribbons
544 (magenta) within cone pedicles (gray) from WT and G369i KI mice. ***b,*** 3D renderings show ribbon
545 sites in a WT cone pedicle contacting one horizontal (HC1; yellow) and three bipolar cells (BC1-
546 3; purple). ***b',*** Raw image from *b* shows a single plane example of BC1-2 and HC1 contacting
547 the ribbon site. ***c-d'***, Single plane raw (*c,d*) images and 3D reconstructions (*c',d'*) show ribbon
548 sites within the G369i KI cone pedicle contacting in *c,c'*: horizontal cells (HC1-2) only (upper
549 panels), CBCs (BC1-2) only (lower panels); and in *d,d'*: a glial cell (orange) and an unknown
550 partner. The glial cell completely envelops the pedicle. Inset in *d'* shows glial-contacting ribbon
551 site (arrow). In other panels, arrows indicate points of contact between ribbons and other
552 postsynaptic elements.
553

554 **Figure 8. Patch clamp recordings of light responses of horizontal cells in WT, G369i KI and**
555 **Ca_v1.4 KO mice. *a-b*,** Representative traces from whole-cell patch clamp recordings of horizontal
556 cells held at -70 mV (*a*) and quantified data (*b*) for currents evoked by 1 s light flashes (λ = 410
557 nm) plotted against light intensities. In *b*, peak current amplitudes during (ON Response) and after
558 (OFF Response) the light stimuli were plotted against photon flux per μm^2 ($\Phi_q/\mu m^2$). Data
559 represent mean ± SEM. WT, n = 8; G369i KI, n = 13; Ca_v1.4 KO, n = 8. There was a significant
560 difference in responses of WT, G369i KI, and Ca_v1.4 KO horizontal cells. For ON responses, F(16,
561 216) = 22, p <0.0001 by two-way repeated measures ANOVA, Tukey's multiple comparisons post-
562 hoc test. For OFF responses, F(16, 216) = 13.61, p < 0.0001 by two-way repeated measures
563 ANOVA, Tukey's multiple comparisons post-hoc test. ***c-d*,** Representative traces from horizontal
564 cells held at -70 mV (*c*) and quantified data (*d*) for currents evoked by 1-s light flashes (λ = 410
565 nm, 1.2 x 10^5 $\Phi_q/\mu m^2$) before, during, and after washout of DNQX (20 μM). In *d,* symbols represent
566 responses from individual cells, n = 5 cells for WT and 3 cells for G369i KI, bars represent mean
567 ± SEM. **, p < 0.01 by paired t-tests.
568
569 **Figure 9. Ca^{2+} imaging of cone terminals in WT and G369i KI mice.** Depolarization-evoked
570 fluorescence changes (ΔF) were measured by two-photon imaging of Fluo3-filled cone pedicles
571 labeled with PNA-Alexa 568. ***a*,** Representative images at the indicated timepoints (T) before
572 (control), during, and after (wash) bath application of KCl (50 mM) and KCl+ISR (10 μM). For
573 clarity, PNA-Alexa 568 labeling was outlined (magenta, solid circles) and the actual labeling only
574 shown in the initial panel of images. Dashed, yellow circles represent ROIs for analyses. ***b*,**
575 Changes in cone pedicle Fluo3 fluorescence were normalized to the initial fluorescence intensity
576 at time= 0 ($\Delta F/F_0$). Solid lines and shaded areas represent the mean $\pm$ SEM, respectively. WT, n
577 = 11 pedicles; G369i KI, n = 14 pedicles.
578

579 **Figure 10. Characterization of ERGs and visual behavior in WT, G369i KI, and Ca_v1.4 KO**
580 **mice.** ***a***, Representative traces of photopic ERGs recorded in the presence of background green
581 light (20 cd · s/m^2) in WT, G369i KI and Ca_V1.4 KO mice. Flash intensities are shown at left.
582 Arrows and arrowheads depict the a- and b-waves, respectively. ***b***, a-wave (left) and b-wave
583 (right) amplitudes are plotted against light intensity. Symbols and bars represent mean ± SEM.
584 WT, n = 7; G369i KI, n = 5; Ca_V1.4 KO, n = 6. *, $p < 0.05$; **, $p < 0.01$; ***, $p < 0.001$; ****, $p <$
585 0.0001; ns, not significant; Two-way ANOVA with Tukey's posthoc multiple comparisons. ***c,d***,
586 Representative traces (*c*) and quantified data (*d*) for 10 Hz flicker responses evoked by white light
587 flashes of increasing luminance (from -4 to 2 log cd· s/m^2). Arrows in *c* depict inverted waveform
588 responses in G369i KI mice that are absent in Ca_v1.4 KO mice. Symbols and bars represent mean
589 ± SEM. WT, n = 7; G369i KI, n = 5; Ca_V1.4 KO, n = 6. *, $p < 0.05$; **, $p < 0.01$. Two-way ANOVA
590 with Tukey's posthoc multiple comparisons. ***e,*** Representative swim path traces of WT, G369i KI
591 and Ca_V1.4 KO mice from the visible platform swim tests performed in the dark (scotopic, upper
592 panel) and light (photopic, lower panel). ***f,*** Time required to reach the platform (latency to platform)
593 was compared for each mouse strain. Symbols represent the average of the last 3 swim trials for
594 each mouse of each genotype for both dark and light conditions. Dotted lines represent the mean.
595 WT, n = 11; G369i KI, n = 10; Ca_V1.4 KO, n = 9. *, $p < 0.05$; ***, $p < 0.001$; ****, $p < 0.0001$;
596 Kruskal-Wallis one-way ANOVA with Dunn's post hoc analysis.
597

598 **Methods**

599 **Table 3. Key resources used in this study.**

Primary Antibodies				
Antibody Name (clone/designation)	**Working Concentration**	**Source**	**Identifier**	**RRID**
Bassoon (SAP7F407/Ms monoclonal)	2 µg/mL	ThermoFisher Scientific	MA1-20689	AB_2066981
Ca_V1.4 (Rb Polyclonal)	5 µg/mL	Amy Lee	Ab167	AB_2650487
Cone Arrestin (Rb Polyclonal)	1 µg/mL	Millipore	AB15282	AB_1163387

Cone Arrestin-CF647 (Rb Polyclonal)	5 µg/mL	Millipore	AB15282	AB_1163387
CtBP2 (Clone 16/Ms Monoclonal)	1 µg/mL	BD Biosciences	612044	AB_399431
GPR179 (mAB 1a/Ms Monoclonal)	2 µg/mL	Millipore	MAB427	AB_2069582
mGluR6 (366/Ms Monoclonal)	1 µg/mL	Dr. Theodore Wensel (Agosto et al., 2014, 2018)	N/A	N/A
TRPM1 (545H5/Ms Monoclonal)	1 µg/mL	Dr. Theodore Wensel (Agosto et al., 2018)	N/A	N/A
Secondary Antibodies				
Antibody Name and Conjugate	**Working Concentration**	**Source**	**Identifier**	**RRID**
Goat Anti-Mouse IgG1 Alexa Fluor 488	4 µg/mL	ThermoFisher	A-21121	AB_2535764
Goat Anti-Mouse IgG2a Alexa Fluor 555	4 µg/mL	ThermoFisher	A-21137	AB_2535776
Goat Anti-Rabbit Alexa Fluor 555	4 µg/mL	ThermoFisher	A-21429	AB_2535850
Goat Anti-Rabbit Alexa Fluor 647	4 µg/mL	ThermoFisher	A-21245	AB_2535813

Chemicals

Reagent or Resource	**Source**	**Identifier**
Adenosine 5'-triphosphate magnesium salt	SIGMA	A9187
Agarose, low gelling temperature	Sigma-Aldrich	A0701
AMES	Sigma, US Biological	Sigma: A1420; US Biological: A1372
Antisedan	Zoetis US LLC	10000449
1,2-Bis(2-aminophenoxy)ethane-N,N,N′,N′-tetraacetic acid (BAPTA)	Sigma-Aldrich	A4926
Cadmium Chloride	Sigma	202908
Calcium chloride dihydrate	Sigma-Aldrich	223506
Cesium Chloride	Fisher Bioreagents	BP210
Cesium methanesulfonate	Sigma-Aldrich	C1426
Creatine phosphate, dipotassium salt	EMD Millipore	237911
D-Glucose	Fisher	D16
DL-*threo*-β-Benzyloxyaspartic acid (DL-TBOA)	Tocris	1223
6,7-Dinitroquinoxaline-2,3-dione disodium salt (DNQX)	Abcam	ab120169
Dimethyl sulfoxide	SIGMA	D2650
Dulbecco's Modified Eagle Medium, high glucose	Gibco	11965-092
Dulbecco's Phosphate Buffered Saline, no calcium, no magnesium	Gibco	14190-144
Ethylene glycol-bis(2-aminoethylether)-N,N,N',N'-tetraacetic acid (EGTA)	Sigma-Aldrich	03777
Fetal Bovine Serum (FBS)	Gibco	16140-071
FuGENE HD Transfection reagent	Promega	E2311
Guanosine 5'-triphosphate sodium salt hydrate	Sigma-Aldrich	G8877
4-(2-Hydroxyethyl)piperazine-1-ethanesulfonic acid (HEPES)	SIGMA	H3375
Systane Hypromellose lubricant eye gel	Alcone	300650474016
Isradipine	Sigma-Aldrich	I6658
Ketamine Injection C IIIN 100 mg/mL	Dechra Veterinary Products, LLC	17033-100-10

Magnesium Chloride hexahydrate	SIGMA	M2393
Methanesulfonic acid	Sigma-Aldrich	471356
Mix-n-Stain Antibody Labeling Kit	Biotium	92238
ML218 Hydrochloride	Tocris	4507
N-Methyl-D-glucamine (NMDG)	Sigma-Aldrich	66930
Nickel Chloride	Sigma	339350
Optimal Cutting Temperature compound	Sakura	4583
Penicillin-Streptomycin	Sigma-Aldrich	P0781
Picrotoxin	Tocris	1128
Sigmacote	Sigma-Aldrich	SL2-25mL
Sodium Bicarbonate	MACRON	7412-12
Sodium phosphate monobasic anhydrous	Sigma	S3139
Sodium phosphate dibasic anhydrous	Sigma	RDD022
Sodium Chloride, Crystal	MACRON	7581-12
Potassium Chloride	Fisher Chemical	P217
Sodium hydroxide	Fisher chemical	S318
Sodium lactate	Sigma-Aldrich	1614308
Sodium malate	Sigma-Aldrich	1613881
Sodium pyruvate	Sigma-Aldrich	P2256
Sodium succinate	Sigma-Aldrich	S9637
Strychnine HCl	Sigma	S8753
(3*S*)-3-[[3-[[4-(Trifluoromethyl)benzoyl]amino]phenyl]methoxy]-L-aspartic acid (TBF-TBOA)	Tocris	2532
Tetraethylammonium chloride (TEA-Cl)	Sigma-Aldrich	86614
TRIS	VWR	0497
Tropicamide ophthalmic solution 1%	Akorn, Inc.	17478-0102-12
Trypsin-EDTA (0.05%), phenol red	Gibco	25300054
Anased (Xylazine) Injection 100 mg/mL	Pivetal	46066-0750-02
4-Ethylphenylamino-1,2-dimethyl-6-methylaminopyrimidinium chloride (ZD7288)	Tocris	1000

Experimental Models: Organisms/Strains

Reagent or Resource	Source	Identifier	RRID
HEK293T	ATCC	CRL-3216	CVCL_0063
Mouse: C57BL/6J	Jackson Labs	000664	IMSR_JAX:000664
Mouse: G369i KI	A. Lee [19]	N/A	N/A
Mouse: $Ca_V1.4$ KO	Jackson Labs	017761	IMSR_JAX:017761
Ground Squirrel	TLC	--	--

Software and Algorithms

Reagent or Resource	Source	Identifier
Amira	ThermoFisher Scientific	https://www.thermofisher.com/amira
cellSens	Olympus	https://www.olympus-lifescience.com/en/software/cellsens
Espion software	Diagnosys, Inc.	https://info.diagnosysllc.com/software
FLUOVIEW	Olympus	https://www.olympus-lifescience.com/en/laser-scanning/fv3000
GraphPad Prism	GraphPad	https://www.graphpad.com
IGOR Pro	WaveMetrics	https://www.wavemetrics.com
ImageJ	NIH	https://imagej.nih.gov/ij
pClamp	Molecular Devices	https://www.moleculardevices.com
Patchmaster	Harvard Bioscience, Inc.	https://www.heka.com

ScanImage	MBF Biosciences	https://docs.scanimage.org/index.html

600

601

602 **Animals**

603 All mouse and macaque experiments were performed in accordance with guidelines
604 approved by the National Institutes of Health and the Institutional Animal Care and Use
605 Committees at the University of Texas at Austin. All ground squirrel (*Ictidomys tridecemlineatus*)
606 procedures performed at Northwestern University were approved by the Institutional Animal Care
607 and Use Committee. The G369i KI [19] and $Ca_v1.4$ KO mouse strains were bred on the C57BL6/J
608 background strain for at least 10 generations. Adult male and female mice were used (6-12 weeks
609 old), and aged-matched C57BL6/J mice were used as the control (WT) animals.

610

611 **Immunofluorescence**

612 Mice between 6-8 weeks of age were anesthetized using isoflurane and euthanized by
613 cervical dislocation. Eyes were enucleated and hemisected. The eye cups with retina were fixed
614 on ice in 4% paraformaldehyde in 0.1 M phosphate buffer (PB) for 30 min. Fixed eye cups were
615 then washed three times with 0.1 M PB containing 1% glycine followed by infusion of 30% sucrose
616 at 4°C overnight. The eye cups were orientated along their dorsal-ventral axis and frozen in a 1:1
617 (wt/vol) mixture of Optimal Cutting Temperature compound and 30% sucrose in a dry
618 ice/isopentane bath. Eye cups were cryosectioned at 20 µm on a Leica CM1850 cryostat (Leica
619 Microsystems), mounted on Superfrost plus Micro Slides (VWR), dried for 5 to 10 min at 42°C,
620 and stored at -20°C until used. Slides with mounted cryosections were warmed to room
621 temperature, washed with 0.1 M PB for 30 min to remove the OCT/sucrose mixture and blocked
622 with dilution solution (DS, 0.1 M PB/10% goat serum/0.5% Triton-X100) for 15 min or overnight
623 at room temperature. All remaining steps were carried out at room temperature. All primary
624 antibodies and appropriate secondary antibodies were diluted in DS at concentrations specified

625 in the Key Resources Table (Table 3). Sections were incubated with primary antibodies for 1 h or
626 overnight and then washed five times with 0.1 M PB. Sections were then incubated with secondary
627 antibodies for 30 min and then washed five times with 0.1 M PB. Trace 0.1 M PB was removed,
628 and sections were then mounted with #1.5H coverslips (ThorLabs) using ProLong Glass Antifade
629 Mountant with or without NucBlue (Thermo Fisher Scientific).

630 For double labeling with other rabbit polyclonal antibodies, CAR antibodies were
631 conjugated with the CF647 fluorophore (CAR-647) using the Mix-n-Stain antibody labeling kit
632 according to the manufacturer's protocol (Biotium). Sections were processed first with rabbit
633 polyclonal $Ca_v1.4$ or EAAT2 antibodies and corresponding secondary antibodies as described
634 above. To prevent CAR-647 from binding to any available sites on the anti-rabbit secondary
635 antibodies previously added to the sections, $Ca_V1.4$ or EAAT2 antibodies were readded to the
636 sections and incubated for 30 min. After washing, the sections were incubated with CAR-647 for
637 1 h, followed by wash steps and cover glass mounting.

638 Immunofluorescence in labeled retinal sections was visualized using an Olympus FV3000
639 confocal microscope (Tokyo, Japan) equipped with an UPlanApo 60x oil HR objective (1.5 NA).
640 Images were captured using the Olympus FLUOVIEW software package. Acquisition settings
641 were optimized using a saturation mask to prevent signal saturation prior to collecting 16-bit. All
642 confocal images presented are maximum z-projections. Images (256 x 256 pixels) used in
643 analyses of synaptic proteins were collected using a 30X optical zoom, 0.6 Airy disk aperture, and
644 voxel size of $0.028\,\mu m \times 0.028\,\mu m \times 0.2\,\mu m$ $(X \times Y \times Z)$. Amira segmentation was used for
645 generating 3D binary masks, and Amira 3D label analysis was used for quantification of
646 immunofluorescent and masked images. Non-deconvolved images were used for all analyses.
647 3D binary masks of individual CAR-labeled pedicles were made by setting the threshold 1
648 standard deviation above mean fluorescence intensity of each 3D image. 3D binary masks of
649 presynaptic labels (CtBP2, $Ca_V1.4$, and Bassoon) or postsynaptic labels (GPR179, mGluR6, and
650 TRPM1) within or associated with the pedicle, respectively, were made by setting the threshold 3

651 standard deviations above the mean fluorescence intensity. To aid in presentation, high-mag
652 images displayed in Figs.1b and 6a were deconvolved using cellSens software (Olympus), and
653 any immunofluorescence corresponding to rod synaptic proteins was subtracted from the image.
654

655 **Molecular biology and transfection**

656 The cDNAs for $Ca_V1.4$ (GenBank: NM_019582), β_{2X13} (GenBank: KJ789960), and $\alpha_2\delta$-
657 4 (GenBank: NM_172364) were previously cloned into pcDNA3.1 [66]. The cDNA for $Ca_V3.2$
658 (GenBank: AF051946) was a gift from Dr. Edward Perez-Reyes, University of Virginia. All
659 constructs were verified by DNA sequencing before use. Human embryonic kidney 293T
660 (HEK293T) cells were cultured in Dulbecco's Modified Eagle's Medium with 10% FBS at 37°C in
661 5% CO_2. At 70–80% confluence, the cells were co-transfected with cDNAs encoding human
662 $Ca_v1.4$ (1.8 μg) β_{2X13} (0.6 μg), $\alpha_2\delta$-4 (0.6 μg), and enhanced GFP in pEGFP-C1 (Clonetech, 0.1
663 μg) or $Ca_V3.2$ (2 μg) and pEGFP-C1 (0.1 μg) using FuGENE 6 transfection reagent according to
664 the manufacturer's protocol. Cells treated with the transfection mixture were incubated at 37°C
665 for 24 hr, dissociated using Trypsin-EDTA, and replated at a low density to isolate single cells.
666 Replated cells were then incubated at 30°C or 37°C for an additional 24 hr before beginning
667 experiments.
668

669 **Solutions for patch clamp recordings**

670 HEK293T extracellular recording solution contained the following (in mM): 140 Tris, 20
671 $CaCl_2$, 1 $MgCl_2$, pH 7.3 with methanesulfonic acid, osmolarity 309 mOsm/kg. HEK293T internal
672 recording solution contained the following: 140 NMDG, 10 HEPES, 2 $MgCl_2$, 2 Mg-ATP, 5 EGTA,
673 pH 7.3 with methanesulfonic acid, osmolarity 358 mOsm/kg.
674 For recordings of I_{Ca} in mouse retina, extracellular recording solution contained the
675 following (in mM): 115 NaCl, 2.5 KCl, 22.5 $NaHCO_3$, 1.25 NaH_2PO_4, 2 $CaCl_2$, 1 $MgCl_2$, 5 HEPES,

676 5 CsCl, 5.5 Glucose, osmolarity 290 mOsm/kg. Mouse cone intracellular solution contained the
677 following (in mM): 105 $CsMeSO_4$, 20 TEA-Cl, 1 $MgCl_2$, 11 HEPES, 10 EGTA, 4 Mg-ATP, 10
678 phosphocreatine, 0.3 Na-GTP, pH 7.4 with CsOH, osmolarity 300 mOsm/kg.

679 For recordings of I_{Ca} in ground squirrel retina, extracellular recording solution contained
680 the following (in mM): 10 HEPES, 85 NaCl, 3.1 KCl, 2.48 $MgSO_4$, 6 Glucose, 1 Na-succinate, 1
681 Na-malate, 1 Na-lactate, 1 Na-pyruvate, 2 $CaCl_2$, 25 $NaHCO_3$, and 20 TEA-Cl, osmolarity 285 ±
682 5 mOsm/kg. Intracellular solution contained the following (in mM): 80 CsCl, 10 BAPTA, 2 $MgSO_4$,
683 10 HEPES, 20 TEA-Cl, 5 Mg-ATP, and 0.5 Na-GTP, pH 7.35 with CsOH, osmolarity 285 ± 5
684 mOsm/kg. For recordings of I_{Aglu}, extracellular recording solution contained (in mM): 125 NaCl,
685 3.0 KCl, 1.25 NaH_2PO_4, 25 $NaHCO_3$, 2 $CaCl_2$, 1 $MgCl_2$, 3 dextrose, 3 sodium pyruvate, 0.1
686 picrotoxin and 0.02 DNQX, and in indicated experiments 0.0013 TFB-TBOA. Intracellular I_{Aglu}
687 contained (in mM): 125 KSCN, 10 TEA-Cl, 10 HEPES, 1 $CaCl_2$, 2 $MgCl_2$, 0.3 Na-GTP, 4 Mg-
688 ATP, 10 K_2 phosphocreatine, 0.02 ZD7288. Mouse and ground squirrel extracellular slice
689 recording solutions were equilibrated with 5% CO_2 / 95% O_2 to a pH of ~7.5.

690 For recordings of light responses in horizontal cells of mouse retina, extracellular
691 recording solution consisted of Ames' media supplemented with 100 U/mL penicillin, 0.1 mg/mL
692 streptomycin and 22.6 mM $NaHCO_3$, osmolarity 280 ± 5 mOsm/kg. The intracellular recording
693 solution contained the following (in mM): 135 K-Aspartate, 10 KCl, 10 HEPES, 5 EDTA, 0.5
694 $CaCl_2$, 1 Mg-ATP, 0.2 Na-GTP, pH 7.35 with KOH, osmolarity 305 ± 5 mOsm/kg.

695

696 **Table 4. Pharmacological drugs and their concentrations used in electrophysiological**
697 **recordings of cones.**
698

Compound	Concentration (μM) for mouse recordings	Concentration (μM) for ground squirrel recordings
Cadmium	200	N/A
DL-TBOA	N/A	375
DNQX	20	N/A
Isradipine	1	2

ML218	5	5
Nickel	100	N/A
Picrotoxin	N/A	50
Strychnine	N/A	10
ZD7288	N/A	50
Glutamate	1000	N/A

699

700 **Patch clamp electrophysiology**

701 Whole-cell voltage clamp recordings of transfected HEK293T cells were performed 48 to
702 72 hrs after transfection using an EPC-10 amplifier and Patchmaster software (HEKA Elektronik,
703 Lambrecht, Germany). Patch pipette electrodes with a tip resistance between 4 and 6 MΩ were
704 pulled from thin-walled borosilicate glass capillaries (World Precision Instruments, Sarasota, FL)
705 using a P-97 Flaming/Brown Puller (Sutter Instruments, Novato, CA). A reference Ag/AgCl wire
706 was placed into the culture dish mounted on an inverted Olympus IX70 microscope. Recordings
707 were performed at room temperature. A pressurized perfusion pencil multi-barrel manifold
708 controlled with Valve Bank II (AutoMate Scientific, Inc., Berkeley, CA) was used to deliver
709 extracellular solutions. ML218 of different concentrations (0.5, 1, 5, 25 and 100 mM) was added
710 to the extracellular solution the day of experiments. Series resistance was compensated up to
711 70%, and passive membrane leak subtraction was conducted using a P/−4 protocol. Whole-cell
712 Ca^{2+} currents (I_{Ca}) of transfected HEK293T cells were evoked for 50 ms with incremental +5 mV
713 steps from -80 mV to +65 mV. Current-Voltage (IV) data were fit with a single Boltzmann equation:
714 $I_{Ca} = G_{max}(V_m-V_r)/(1+\exp[-(V_m-V_h))/k])$, where G_{max} is the maximal conductance, V_m is the test
715 voltage, V_r is the Ca^{2+} reversal potential, V_h is the membrane potential required to activate 50%
716 of G_{max}, and k is the slope factor. Data were sampled at 100 kHz, filtered at 3 kHz, and analyzed
717 using custom programs written in IgroPro (WaveMetrics).

718 Whole-cell voltage clamp recordings of mouse cones, macaque cone terminals, and
719 mouse horizontal cells were performed using an EPC-10 amplifier and Patchmaster software
720 (HEKA). Patch pipette electrodes with a tip resistance between 10 and 14 MΩ for cones and 6-8

721 for horizontal cells were pulled from thick-walled borosilicate glass (1.5 mm outer diameter; 0.84
722 mm inner diameter; World Precision Instruments).

723 To prepare retinal slices, adult mice (6 – 8 weeks old) were anesthetized using isoflurane
724 and euthanized by cervical dislocation. Eyes were enucleated, placed into cold Ames' media
725 slicing solution, and hemisected. Following removal of the vitreous, the eye cup was separated
726 into dorsal and ventral halves using a scalpel. Ventral retina was isolated, molded into low-melt
727 agarose and mounted in a Leica VT1200s vibratome (Leica Biosystems). Mouse retina slicing
728 solution was continuously bubbled with 100% O_2 and contained the following: Ames' Medium with
729 L-glutamine supplemented with (in mM) 15 NaCl, 10 HEPES, 10 U/mL penicillin, 0.1 mg/mL
730 streptomycin, pH 7.4, osmolarity 300 mOsm/kg. Vertical (~200 μm) or horizontal (~160 μm) retinal
731 slices were anchored in a recording chamber, placed onto a fixed stage, and positioned under an
732 upright Olympus BX51WI microscope equipped with a 60X water-immersion objective (1.0 NA),
733 and superfused with extracellular solution (flow rate of ~1-2 ml/min) at room temperature. Slices
734 were visualized using IR-DIC optics and an IR-2000 (Dage MTI, Michigan City, IN) or SciCam Pro
735 (Scientifica, Uckfield, United Kingdom) CCD camera controlled by the IR-capture software
736 package or μManager, respectively [67, 68]. Drugs used in these experiments were added to the
737 mouse extracellular solution the day of experiments at the concentration described in Table 4. A
738 reference Ag/AgCl pellet electrode was placed directly into the recording chamber solution. Data
739 from whole-cell recordings with a series resistance >20 MΩ were discarded.

740 Cone somas were identified based on their morphology and location (outer ONL cell
741 layer). Cone identity was confirmed by the whole-cell capacitance (~3-4 pF), which is larger than
742 rod whole-cell capacitance (~0.7-1 pF). For cone voltage ramp recordings, cones were held at -
743 90 mV for 200 ms followed by a ramp of +0.5 mV/ms to +40 mV. To determine voltage activation
744 of I_{Ca}, whole-cell Ca^{2+} currents in cones were evoked for 50 ms with incremental +5 mV steps
745 from -80 mV to +40 mV. The activation voltage of I_{Ca} is reported as G/G_{max}, where G is the
746 conductance at each test voltage and G_{max} is the maximum peak conductance for each cone.

747 Conductance was calculated using the equation $I_{Ca} = G(V_m - V_r)$, where V_r is +60 mV. To determine
748 steady state inactivation of I_{Ca}, currents in cones were evoked for 500 ms with incremental +5 mV
749 steps from -90 mV and -30 mV followed by a final step to -30 mV for 50 ms after each test voltage.
750 The steady state inactivation of I_{Ca} is reported as I/I_{max}, where I is the peak current in the final
751 voltage step to -30 mV and I_{max} is the maximum peak current for each cone. Data were sampled
752 between 20 and 60 kHz and filtered at 3 kHz.

753 For horizontal cell light responses, horizontal slices were prepared from central mouse
754 retina. The identity of horizontal cells was determined based on their larger soma diameter (~15
755 μm) compared to bipolar cell somas (~6 μm). During whole cell patch clamp recordings, horizontal
756 cells were held at -70 mV. Light stimuli (1 s) at 410 nm (630 x 830 μm) were presented onto the
757 retina (at a minimum of 5 s intervals) through the microscope's condenser using a Polygon1000
758 DMD pattern illuminator (Mightex, Pleasanton, CA, USA) and a custom-built light path. Light
759 intensity (in watts) was measured at the point on the microscope stage where the retina is placed
760 using a power meter (Thorlabs, Newton, New Jersey, USA). Photon flux Φ_q (photons/s) within the
761 light stimulus area was calculated using the measured light intensities in the formula:

762 $$\Phi_q \text{ per } \mu m^2 = \frac{measured\ light\ intensity\ (W)}{\frac{hc}{\lambda}} / light\ stimulus\ area\ (\mu m^2)$$

763 where h is Planck's constant (J*s), c is the speed of light (m/s), and λ is the wavelength (m). Light
764 stimulus intensity was increased in Log2 steps from 4.9×10^2 to 2.1×10^5 $\Phi_q/\mu m^2$. For each light
765 intensity step, both ON and OFF current amplitudes were measured from baseline (averaged 5
766 ms of current prior to light onset) to the maximum positive (after light onset) or maximum negative
767 (after light offset) current, respectively. To confirm the identity of these horizontal cell light

768 responses as AMPA-mediated currents, 1 s light stimuli (410 nm, 1.2×10^5 $\Phi_q/\mu m^2$) were
769 continuously delivered every 10 s before, during and after bath application of 20 μM DNQX.
770 For voltage clamp recordings of 13-lined ground squirrel cones, retinal slices were
771 prepared as previously described [69]. The eyecup was divided along the dorsal to ventral axis into
772 superior, middle, and inferior parts. The dorsal area above the line of the optic nerve head was
773 defined as superior, the central region with a width of about 5 mm just ventral to the optic nerve
774 head was middle, and the remaining ventral area was inferior. Isradipine and ML218, alone or in
775 combination, were applied from separate puffer pipettes whose orifices were aimed at the cone
776 synaptic region. Recordings were made with an Axopatch 200B amplifier (Molecular Devices).
777 Signals were electronically filtered at 5 kHz and digitized at a rate of 10 kHz. Additional Gaussian
778 filtering was added (cutoff frequency of 500 Hz). Tissue was viewed through a 63x water
779 immersion objective on a Zeiss Axioskop FS2 microscope and superfused with extracellular
780 solution at room temperature. Drugs and their concentrations used during these experiments are
781 described in Table 4. Membrane potential was continuously maintained at -85 mV. During ramp
782 stimulation, the membrane potential was depolarized to -85 to +35 mV at a rate of 1 mV/ms.
783 For rhesus macaque cone terminal recordings, a 12-year-old male was sedated with
784 ketamine (5 mg/kg I.M.) and dexmedetomidine (0.015 mg/kg I.M.). Post-sedation, the animal
785 received buprenorphine (0.02 mg/kg I.M.), atropine (0.02 mg/kg I.M.), and maropitant citrate (1
786 mg/kg S.Q.). The animal was intubated and maintained with inhaled isoflurane (0.75-2.0%) and
787 propofol (7-8 mg/kg/hr I.V.). Crystalloid fluids (5 mL/kg/hr) were administered I.V., and
788 phenylephrine (5-10 mcg/kg/hr I.V.) was used for blood pressure support. The animal was under
789 anesthesia for approximately 3 hours prior to perfusion. Transcardial perfusion was approached
790 through a midline thoracotomy. Immediately prior to perfusion, 5 mL of Euthasol® (sodium
791 pentobarbital 390 mg/mL/phenytoin sodium 50 mg/mL) was administered I.V. The descending
792 thoracic aorta was clamped, the pericardium was opened, and the right atrium was cut. The apex

793 of the left ventricle was sharply incised, and a large bore cannula (Yankauer suction handle, 5
794 mm internal diameter) was inserted through the left ventricle until it could be palpated in the
795 ascending aorta. The cannula was clamped in place at the apex of the left ventricle. The animal
796 was perfused with 4 L of cold phosphate-buffered saline at ~500 mL/min. Eyes were removed
797 approximately 1 hour following perfusion. Eyes were dissected, and eye cups were allowed to
798 dark adapt for ~30 min and stored in bicarbonate buffered Ames' media at 32°C equilibrated with
799 95% O_2/5% CO_2 prior to slice preparations. Vertical sections of central retina were prepared from
800 5 mm retina punches as described for mice.
801
802 **Single cell RNA sequencing**
803 Retinas from 2 WT and 2 G369i KI mice (2-3 month old, all males) were dissected in ice-
804 cold Dulbecco's Phosphate Buffered Saline (D-PBS) and dissociated into single cells using the
805 Papain Dissociation System (Worthington Biochemical). Two retinas were incubated in a 2.5 ml
806 of dissociation solution (40 U/ml papain, 2 mM L-cysteine, 200 U/ml DNAse in Earle's Balanced
807 Salt Solution, EBSS) for 8 min at 37 °C. Following aspiration, 2 ml of inactivation solution
808 (ovomucoid protease inhibitor and bovine serum albumin (BSA), 10 mg/ml each in EBSS) was
809 added prior to trituration with a series of fire-polished, siliconized glass Pasteur pipettes. The
810 solution was passed through a 40 μm mesh (pluriStrainer, Cat# 43-50040-51, pluriSelect) prior to
811 centrifugation (200 x *g* for 5 min, 4 °C). Following aspiration of the supernatant, the cell pellet was
812 resuspended in 0.5 ml D-PBS+0.5% BSA. Cell suspensions (10,000 cells per sample) were
813 loaded on the Chromium Controller (10X Genomics) and processed for cDNA library generation
814 following the manufacturer's instructions for the Chromium NextGEM Single Cell 3' Reagent Kit
815 v3.1 (10X Genomics). The resulting libraries were examined for size and quality using the
816 Bioanalyzer High Sensitivity DNA Kit (Agilent) and their concentrations were measured using the

817 KAPA SYBR Fast qPCR kit (Roche). Samples were sequenced on the NovaSeq 6000 instrument
818 (paired end, read 1: 28 cycles, read 2: 90 cycles) with a targeted depth of 9K reads/cell.
819 scRNA-seq Fastq files were processed with CellRanger (v7.1.0) using the reference
820 genome mm10–2020-A with introns included. CellRanger outputs were imported to Seurat
821 (v5.0.1), gene by feature count matrix was constructed, log normalization was performed, and the
822 log normalized values were used for downstream analysis. Unsupervised clustering was
823 performed in Seurat using resolution=0.5. DEsingle method (v1.6.0, [70]) was used for differential
824 expression analysis comparing G369i KI to WT in each cluster.
825
826 **Serial block-face scanning electron microscopy and 3D reconstructions**
827 Eye cups were prepared from P42 WT and G369i KI littermates and fixed using 4%
828 glutaraldehyde in 0.1M cacodylate buffer, pH 7.4, for 4 hours at room temperature followed by
829 additional fixation overnight at 4°C. Glutaraldehyde-fixed eye cups were then washed 3 times in
830 0.1M cacodylate buffer. Retinas were thereafter isolated and embedded in Durcupan resin after
831 staining, dehydration, and embedding as described previously (Della Santina et al., 2016). A
832 Thermo Scientific VolumeScope serial block face scanning electron micrscope was used to image
833 embedded retinas. Retinal regions comprising a 2x2 montage of 40.96 μm tiles were imaged at a
834 resolution of 5nm/pixel and section thickness of 50 nm. Image stacks were aligned, and cone
835 photoreceptor terminals reconstructed using TrakEM2 (NIH). Postsynaptic partners at cone
836 ribbons were followed to the inner nuclear layer to determine their identity. Amira software was
837 used for 3D visualization of reconstructed profiles.
838
839 **Electroretinography**
840 Retinal function was assessed using the Celeris system (Diagnosys, Inc.) paired with the
841 Espion software (Diagnosys, Inc.). Mice were anaesthetized under red light (660 nm) via
842 intraperitoneal (I.P.) injection with ketamine/xylazine mixture (100 mg/kg ketamine, 10 mg/kg

843 xylazine). Tropicamide ophthalmic solution (1 %) and hypromellose lubricant eye gel (0.3 %) were
844 administered topically to both eyes before the mouse was secured to a heated (37 °C) platform
845 to maintain body temperature. Ag/AgCl corneal stimulators were placed on each eye. After
846 collecting data from individual mice, atipamezole (Antisedan, 1-2 mg/kg) was I.P. injection
847 administered to reverse the effects of the ketamine and xylazine. For photopic ERGs, eyes were
848 light adapted using a background green light at 20 cd·s/m^2 for 10 min. Following light adaptation,
849 eight different light intensity pulses (-0.5, 0, 0.5, 1, 1.5, 2, 2.3 and 2.6 log cd·s/m^2) were delivered
850 on top of the background green light. ERG a-waves were measured from baseline to the peak of
851 the negative potential. ERG b-waves were measured without filtering the oscillatory potentials
852 from the peak of the a-wave to the peak of the positive potential within 60- 70 ms (WT) and 80-
853 100 ms (G369i KI and $Ca_V1.4$ KO) of the light stimuli. For flickering ERGs, mice were dark adapted
854 (>12 h). White light pulses from -4 to 2.5 log cd·s/m^2 were delivered in 0.5 log unit steps at 10 Hz.
855 Response amplitudes were measured from the trough to the peak of each response at all light
856 intensities. Each intensity stimulus was delivered 10 times, with a 3 s interval between each
857 stimulus, and averaged. The mean response amplitudes recorded in the right and left eye of each
858 mouse are reported for all quantified ERG data.
859
860 **Visible platform swim test**
861 The visible platform swim test was performed as has been previously described [31]. WT,
862 G369i KI, and $Ca_v1.4$ KO male and female mice (6- 9 weeks old) were dark-adapted overnight
863 and allowed to adapt to the procedure room for at least 1 h prior to beginning the experiments. A
864 water-filled, 4-foot diameter galvanized steel tank and a visible white platform with a diameter of
865 10 cm was used for the swim test. Mice were subjected to 6 swim trials per day. Assays conducted
866 under photopic (55 lux) and scotopic conditions (0 lux) were performed on days 1 and 2,
867 respectively. Light intensity for photopic and scotopic conditions was measured at the platform
868 using an Extech HD450 light meter (FLIR Systems, Nashua, New Hampshire). Mice were given

869 90 s to find the platform before being removed. After one trial was performed on all mice, the
870 platform was moved to one of three different locations, top left, top center, and top right in relation
871 to the initial site of mouse placement in tank. Each trial was recorded using an infrared camera
872 (Basler AG, Ahrensburg, Germany) and EthoVision XT16 software (Noldus Information
873 Technology). Locating the platform was considered successful when mice contacted the platform
874 with a head-on approach, even if mice failed to escape onto the platform. Mice were allowed to
875 rest on the platform for 15 s at the end of each trial before being returned to a pre-warmed cage.
876 Latency to find the platform was manually recorded and confirmed using recorded videos. Male
877 and female mice were tested separately, and no sex differences in performance were identified
878 post-hoc using two-way RM-ANOVA (Supplementary Table 1). Male and female data were
879 combined into a single group for each genotype. Latency to platform was calculated by averaging
880 the final 3 trials under scotopic and photopic conditions for each mouse and compared using
881 Kruskal-Wallis one-way ANOVA with Dunn's posthoc multiple comparison test.
882
883 **Ca^{2+} Imaging of Cone Terminals**
884 Retinas were dissected and stored in oxygenated mouse retina slicing solution. The
885 loading of the cell-permeant Ca^{2+} dye Fluo-3, AM was modified from on a previous publication[71].
886 To label the base of cone terminals, retinas were incubated in retina slicing solution containing
887 PNA Lectin conjugated with CF568 (100 μg/mL) for 15 min at room temperature. Then the retinas
888 were incubated with retina slicing solution containing 1mM Fluo-3, AM and 0.025% pluronic acid
889 (Biotium) for 45 min at room temperature followed by 3 rinses with retina slicing solution. The
890 retinas were then incubated in retina slicing solution for 15 min at 35ºC to increase esterase
891 activity. Vertical retina slices were prepared as described above. Slices were mounted on a
892 Hyperscope multiphoton system (Scientifica, Uckfield, United Kingdom) equipped with a resonant
893 scanner and a Mai Tai HP DeepSee laser (Spectra-Physics, Milpitas, CA, USA) tuned to 800 nm
894 at 5% power. Slices were perfused with normal extracellular solution containing (in mM) 112 NaCl,

895 3 KCl, 1 $MgCl_2$, 3 $CaCl_2$, 1.25 NaH_2PO_4, 10 Na Pyruvate, 22.5 $NaHCO_3$, 5 HEPES, 10 Glucose,
896 osmolarity 300 $\pm$ 5 mOsm/kg. High-K+ extracellular solution contained (in mM) 65 NaCl, 50 KCl,
897 1 $MgCl_2$, 3 $CaCl_2$, 1.25 NaH_2PO_4, 10 Na Pyruvate, 22.5 $NaHCO_3$, 5 HEPES, 10 Glucose,
898 osmolarity 300 $\pm$ 5 mOsm/kg. Extracellular solutions were supplemented with 20 μM CNQX, 25
899 μM L-APV, and 100 μM picrotoxin. Isradipine (10 μM) was added to High-K+ extracellular solution.
900 Images (512x512) were collected as 15-frame averages at 0.93 Hz using ScanImage (MBF
901 Bioscience, Williston, VT, USA). Changes of Fluo-3 fluorescence in cone terminals were
902 measured in ROIs drawn juxtaposed to PNA-CF568 labeling using Fiji[72].
903
904 **Data analysis**
905 Electrophysiological data were analyzed by custom routines written in IgorPro software
906 (Wavemetrics) and statistical analysis was performed using Prism software (GraphPad). Data
907 were analyzed for normality by Shapiro Wilk test followed by parametric (t-test or ANOVA) or non-
908 parametric methods (Kruskal Wallis, Mann-Whitney, Wilcoxon).
909
910 **REFERENCES**
911
912 1. Snellman, J.*, et al.* Acute destruction of the synaptic ribbon reveals a role for the ribbon in
913 vesicle priming. *Nat Neurosci* **14**, 1135-1141 (2011).

914 2. Dembla, E., Dembla, M., Maxeiner, S. & Schmitz, F. Synaptic ribbons foster active zone
915 stability and illumination-dependent active zone enrichment of RIM2 and Cav1.4 in photoreceptor
916 synapses. *Sci Rep* **10**, 5957 (2020).

917 3. Haverkamp, S., Grunert, U. & Wassle, H. The cone pedicle, a complex synapse in the
918 retina. *Neuron* **27**, 85-95 (2000).

919 4. Mercer, A.J. & Thoreson, W.B. The dynamic architecture of photoreceptor ribbon
920 synapses: cytoskeletal, extracellular matrix, and intramembrane proteins. *Vis Neurosci* **28**, 453-
921 471 (2011).

922 5. Frederick, C.E. & Zenisek, D. Ribbon Synapses and Retinal Disease: Review. *Int J Mol*
923 *Sci* **24** (2023).

924 6. Mansergh, F.*, et al.* Mutation of the calcium channel gene Cacna1f disrupts calcium
925 signaling, synaptic transmission and cellular organization in mouse retina. *Hum Mol Genet* **14**,
926 3035-3046 (2005).

927 7. Liu, X.*, et al.* Dysregulation of $Ca_v1.4$ channels disrupts the maturation of photoreceptor
928 synaptic ribbons in congenital stationary night blindness type 2. *Channels* **7**, 514-523 (2013).

929 8. Chang, B.*, et al.* The nob2 mouse, a null mutation in Cacna1f: anatomical and functional
930 abnormalities in the outer retina and their consequences on ganglion cell visual responses. *Vis*
931 *Neurosci* **23**, 11-24 (2006).

932 9. Singh, A.*, et al.* C-terminal modulator controls Ca^{2+}-dependent gating of $Ca_v1.4$ L-type
933 Ca^{2+} channels. *Nat Neurosci* **9**, 1108-1116 (2006).

934 10. Wahl-Schott, C.*, et al.* Switching off calcium-dependent inactivation in L-type calcium
935 channels by an autoinhibitory domain. *Proc. Natl. Acad. Sci. U. S. A.* **103**, 15657-15662 (2006).

936 11. Bech-Hansen, N.T., *et al.* Loss-of-function mutations in a calcium-channel a_1-subunit gene
937 in Xp11.23 cause incomplete X-linked congenital stationary night blindness. *Nature Genet.* **19**,
938 264-267 (1998).

939 12. Strom, T.M., *et al.* An L-type calcium-channel gene mutated in incomplete X-linked
940 congenital stationary night blindness. *Nature Genet.* **19**, 260-263 (1998).

941 13. Waldner, D.M., Bech-Hansen, N.T. & Stell, W.K. Channeling Vision: CaV1.4-A Critical Link
942 in Retinal Signal Transmission. *Biomed Res Int* **2018**, 7272630 (2018).

943 14. Boycott, K.M., Pearce, W.G. & Bech-Hansen, N.T. Clinical variability among patients with
944 incomplete X-linked congenital stationary night blindness and a founder mutation in CACNA1F.
945 *Can J Ophthalmol* **35**, 204-213 (2000).

946 15. Zeitz, C., Robson, A.G. & Audo, I. Congenital stationary night blindness: an analysis and
947 update of genotype-phenotype correlations and pathogenic mechanisms. *Progress in retinal and*
948 *eye research* **45**, 58-110 (2015).

949 16. Regus-Leidig, H., *et al.* Photoreceptor degeneration in two mouse models for congenital
950 stationary night blindness type 2. *PLoS One* **9**, e86769 (2014).

951 17. Zabouri, N. & Haverkamp, S. Calcium channel-dependent molecular maturation of
952 photoreceptor synapses. *PLoS One* **8**, e63853 (2013).

953 18. Raven, M.A., *et al.* Early afferent signaling in the outer plexiform layer regulates
954 development of horizontal cell morphology. *J Comp Neurol* **506**, 745-758 (2008).

955 19. Maddox, J.W., *et al.* A dual role for Cav1.4 Ca(2+) channels in the molecular and structural
956 organization of the rod photoreceptor synapse. *Elife* **9**, e62184 (2020).

957 20. Perez-Reyes, E. Molecular physiology of low-voltage-activated t-type calcium channels.
958 *Physiol Rev* **83**, 117-161 (2003).

959 21. Davison, A., Lux, U.T., Brandstatter, J.H. & Babai, N. T-Type Ca(2+) Channels Boost
960 Neurotransmission in Mammalian Cone Photoreceptors. *J. Neurosci.* **42**, 6325-6343 (2022).

961 22. Koschak, A., *et al.* Cav1.4alpha1 subunits can form slowly inactivating dihydropyridine-
962 sensitive L-type Ca2+ channels lacking Ca2+-dependent inactivation. *J. Neurosci.* **23**, 6041-6049
963 (2003).

964 23. Williams, B., Maddox, J.W. & Lee, A. Calcium Channels in Retinal Function and Disease.
965 *Annu Rev Vis Sci* (2022).

966 24. Martemyanov, K.A. & Sampath, A.P. The Transduction Cascade in Retinal ON-Bipolar
967 Cells: Signal Processing and Disease. *Annu Rev Vis Sci* **3**, 25-51 (2017).

968 25. Hack, I., Frech, M., Dick, O., Peichl, L. & Brandstatter, J.H. Heterogeneous distribution of
969 AMPA glutamate receptor subunits at the photoreceptor synapses of rodent retina. *Eur J Neurosci*
970 **13**, 15-24 (2001).

971 26. Brandstatter, J.H., Koulen, P. & Wassle, H. Selective synaptic distribution of kainate
972 receptor subunits in the two plexiform layers of the rat retina. *J. Neurosci.* **17**, 9298-9307 (1997).

973 27. Feigenspan, A. & Babai, N. Functional properties of spontaneous excitatory currents and
974 encoding of light/dark transitions in horizontal cells of the mouse retina. *Eur J Neurosci* **42**, 2615-
975 2632 (2015).

976 28. Krizaj, D. Calcium stores in vertebrate photoreceptors. *Adv Exp Med Biol* **740**, 873-889
977 (2012).

978 29. Nusinowitz, S., Ridder, W.H., 3rd & Ramirez, J. Temporal response properties of the
979 primary and secondary rod-signaling pathways in normal and Gnat2 mutant mice. *Exp Eye Res*
980 **84**, 1104-1114 (2007).

981 30. Vinberg, F., Wang, T., Molday, R.S., Chen, J. & Kefalov, V.J. A new mouse model for
982 stationary night blindness with mutant Slc24a1 explains the pathophysiology of the associated
983 human disease. *Hum Mol Genet* **24**, 5915-5929 (2015).

984 31. Bimonte-Nelson, H., Daniel, J. & Koebele, S. *The maze book: theories, practice, and*
985 *protocols for testing rodent cognition* (Springer, 2015).

986 32. Beier, C*., et al.* Deafferented Adult Rod Bipolar Cells Create New Synapses with
987 Photoreceptors to Restore Vision. *J. Neurosci.* **37**, 4635-4644 (2017).

988 33. Shen, N., Wang, B., Soto, F. & Kerschensteiner, D. Homeostatic Plasticity Shapes the
989 Retinal Response to Photoreceptor Degeneration. *Curr Biol* **30**, 1916-1926 e1913 (2020).

990 34. Leinonen, H*., et al.* Homeostatic plasticity in the retina is associated with maintenance of
991 night vision during retinal degenerative disease. *Elife* **9** (2020).

992 35. Care, R.A., *et al.* Mature Retina Compensates Functionally for Partial Loss of Rod
993 Photoreceptors. *Cell rep* **31**, 107730 (2020).

994 36. Kiyonaka, S., *et al.* RIM1 confers sustained activity and neurotransmitter vesicle anchoring
995 to presynaptic Ca2+ channels. *Nat Neurosci* **10**, 691-701 (2007).

996 37. Kiyonaka, S., *et al.* Physical and functional interaction of the active zone protein
997 CAST/ERC2 and the beta-subunit of the voltage-dependent Ca(2+) channel. *Journal of*
998 *biochemistry* **152**, 149-159 (2012).

999 38. tom Dieck, S., *et al.* Molecular dissection of the photoreceptor ribbon synapse: physical
1000 interaction of Bassoon and RIBEYE is essential for the assembly of the ribbon complex. *J Cell*
1001 *Biol* **168**, 825-836 (2005).

1002 39. Alpadi, K., *et al.* RIBEYE recruits Munc119, a mammalian ortholog of the Caenorhabditis
1003 elegans protein unc119, to synaptic ribbons of photoreceptor synapses. *J. Biol. Chem.* **283**,
1004 26461-26467 (2008).

1005 40. Haeseleer, F. Interaction and colocalization of CaBP4 and Unc119 (MRG4) in
1006 photoreceptors. *Invest Ophthalmol Vis Sci* **49**, 2366-2375 (2008).

1007 41. Haeseleer, F., *et al.* Essential role of Ca^{2+}-binding protein 4, a $Ca_v1.4$ channel regulator,
1008 in photoreceptor synaptic function. *Nat Neurosci* **7**, 1079-1087 (2004).

1009 42. Schmitz, F., Konigstorfer, A. & Sudhof, T.C. RIBEYE, a component of synaptic ribbons: a
1010 protein's journey through evolution provides insight into synaptic ribbon function. *Neuron* **28**, 857-
1011 872 (2000).

1012 43. tom Dieck, S.*, et al.* Deletion of the presynaptic scaffold CAST reduces active zone size
1013 in rod photoreceptors and impairs visual processing. *J. Neurosci.* **32**, 12192-12203 (2012).

1014 44. Macosko, E.Z.*, et al.* Highly Parallel Genome-wide Expression Profiling of Individual Cells
1015 Using Nanoliter Droplets. *Cell* **161**, 1202-1214 (2015).

1016 45. Koschak, A.*, et al.* a_{1D} ($Ca_v1.3$) subunits can form L-type Ca^{2+} channels activating at
1017 negative voltages. *J. Biol. Chem.* **276**, 22100-22106 (2001).

1018 46. Tringham, E.*, et al.* T-type calcium channel blockers that attenuate thalamic burst firing
1019 and suppress absence seizures. *Sci Transl Med* **4**, 121ra119 (2012).

1020 47. Cai, S., Gomez, K., Moutal, A. & Khanna, R. Targeting T-type/CaV3.2 channels for chronic
1021 pain. *Transl Res* **234**, 20-30 (2021).

1022 48. Garcia-Caballero, A.*, et al.* The deubiquitinating enzyme USP5 modulates neuropathic
1023 and inflammatory pain by enhancing Cav3.2 channel activity. *Neuron* **83**, 1144-1158 (2014).

1024 49. Welsby, P.J.*, et al.* A mechanism for the direct regulation of T-type calcium channels by
1025 Ca2+/calmodulin-dependent kinase II. *J. Neurosci.* **23**, 10116-10121 (2003).

1026 50. Gomez, K.*, et al.* Cdk5-Dependent Phosphorylation of Ca(V)3.2 T-Type Channels:
1027 Possible Role in Nerve Ligation-Induced Neuropathic Allodynia and the Compound Action
1028 Potential in Primary Afferent C Fibers. *J. Neurosci.* **40**, 283-296 (2020).

1029 51. Ingram, N.T., Sampath, A.P. & Fain, G.L. Voltage-clamp recordings of light responses
1030 from wild-type and mutant mouse cone photoreceptors. *J. Gen. Physiol.* **151**, 1287-1299 (2019).

1031 52. Spiwoks-Becker, I., Glas, M., Lasarzik, I. & Vollrath, L. Mouse photoreceptor synaptic
1032 ribbons lose and regain material in response to illumination changes. *Eur J Neurosci* **19**, 1559-
1033 1571 (2004).

1034 53. Regus-Leidig, H., Specht, D., Tom Dieck, S. & Brandstatter, J.H. Stability of active zone
1035 components at the photoreceptor ribbon complex. *Mol Vis* **16**, 2690-2700 (2010).

1036 54. Sheets, L., Kindt, K.S. & Nicolson, T. Presynaptic CaV1.3 channels regulate synaptic
1037 ribbon size and are required for synaptic maintenance in sensory hair cells. *J. Neurosci.* **32**,
1038 17273-17286 (2012).

1039 55. Wong, H.C.*, et al.* Synaptic mitochondria regulate hair-cell synapse size and function. *Elife*
1040 **8** (2019).

1041 56. Goel, P.*, et al.* Homeostatic scaling of active zone scaffolds maintains global synaptic
1042 strength. *J Cell Biol* **218**, 1706-1724 (2019).

1043 57. Hong, H.*, et al.* Structural Remodeling of Active Zones Is Associated with Synaptic
1044 Homeostasis. *J. Neurosci.* **40**, 2817-2827 (2020).

1045 58. Kerov, V.*, et al.* alpha2delta-4 Is Required for the Molecular and Structural Organization
1046 of Rod and Cone Photoreceptor Synapses. *J. Neurosci.* **38**, 6145-6160 (2018).

1047 59. Zanetti, L.*, et al.* Function of cone and cone-related pathways in CaV1.4 IT mice. *Sci Rep*
1048 **11**, 2732 (2021).

1049 60. Knoflach, D.*, et al.* Ca_v1.4 IT mouse as model for vision impairment in human congenital
1050 stationary night blindness type 2. *Channels* **7**, 503-513 (2013).

1051 61. Perez-Reyes, E., Van Deusen, A.L. & Vitko, I. Molecular pharmacology of human Cav3.2
1052 T-type Ca2+ channels: block by antihypertensives, antiarrhythmics, and their analogs. *The*
1053 *Journal of pharmacology and experimental therapeutics* **328**, 621-627 (2009).

1054 62. Choi, S.Y., Jackman, S., Thoreson, W.B. & Kramer, R.H. Light regulation of Ca2+ in the
1055 cone photoreceptor synaptic terminal. *Vis Neurosci* **25**, 693-700 (2008).

1056 63. Bijveld, M.M.*, et al.* Assessment of night vision problems in patients with congenital
1057 stationary night blindness. *PLoS One* **8**, e62927 (2013).

1058 64. Peloquin, J.B., Rehak, R., Doering, C.J. & McRory, J.E. Functional analysis of congenital
1059 stationary night blindness type-2 CACNA1F mutations F742C, G1007R, and R1049W.
1060 *Neuroscience* **150**, 335-345 (2007).

1061 65. Hoda, J.C., Zaghetto, F., Koschak, A. & Striessnig, J. Congenital stationary night
1062 blindness type 2 mutations S229P, G369D, L1068P, and W1440X alter channel gating or
1063 functional expression of Cav1.4 L-type Ca2+ channels. *J. Neurosci.* **25**, 252-259 (2005).

1064 66. Lee, A.*, et al.* Characterization of Cav1.4 complexes ($\alpha_1$1.4, β_2, and $\alpha_2\delta$−4) in HEK293T
1065 cells and in the retina. *J. Biol. Chem.* **290**, 1505-1521 (2015).

1066 67. Edelstein, A., Amodaj, N., Hoover, K., Vale, R. & Stuurman, N. Computer control of
1067 microscopes using microManager. *Curr Protoc Mol Biol* **Chapter 14**, Unit14 20 (2010).

1068 68. Edelstein, A.D.*, et al.* Advanced methods of microscope control using muManager
1069 software. *J Biol Methods* **1** (2014).

1070 69. DeVries, S.H. & Schwartz, E.A. Kainate receptors mediate synaptic transmission between
1071 cones and 'Off' bipolar cells in a mammalian retina. *Nature* **397**, 157-160 (1999).

1072 70. Miao, Z., Deng, K., Wang, X. & Zhang, X. DEsingle for detecting three types of differential
1073 expression in single-cell RNA-seq data. *Bioinformatics* **34**, 3223-3224 (2018).

1074 71. Johnson, J.E., Jr.*, et al.* Spatiotemporal regulation of ATP and Ca2+ dynamics in
1075 vertebrate rod and cone ribbon synapses. *Mol Vis* **13**, 887-919 (2007).

1076 72. Schindelin, J.*, et al.* Fiji: an open-source platform for biological-image analysis. *Nature*
1077 *methods* **9**, 676-682 (2012).
1078

Figure 1

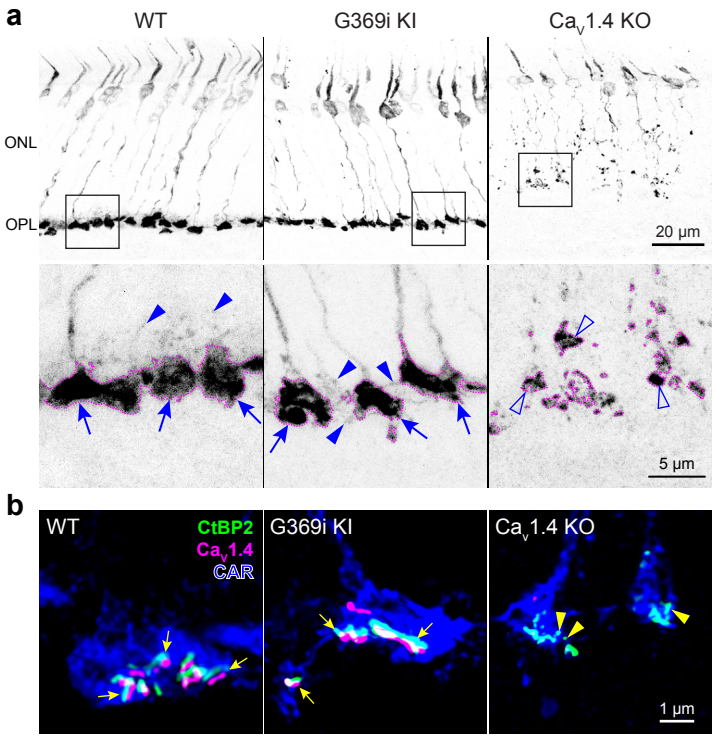
a
WT
G369i KI
Ca$_V$1.4 KO
ONL
OPL
20 µm
5 µm
b
WT
CtBP2
Ca$_V$1.4
CAR
G369i KI
Ca$_V$1.4 KO
1 µm

Figure 2

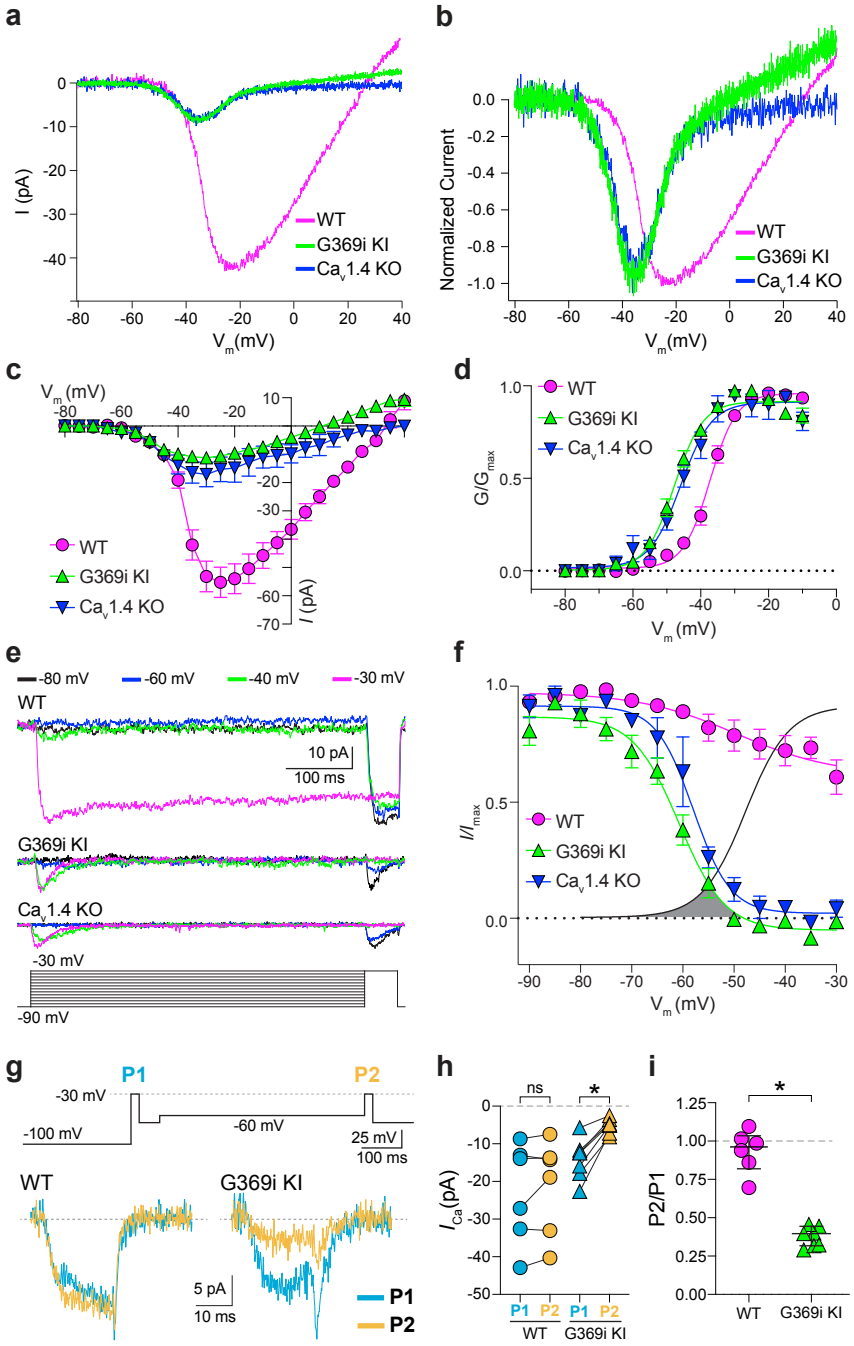
a
I (pA)
WT
G369i KI
Cav1.4 KO
Vm(mV)
b
Normalized Current
WT
G369i KI
Cav1.4 KO
Vm(mV)
c
Vm (mV)
WT
G369i KI
Cav1.4 KO
I (pA)
d
G/Gmax
WT
G369i KI
Cav1.4 KO
Vm (mV)
e
-80 mV
-60 mV
-40 mV
-30 mV
WT
10 pA
100 ms
G369i KI
Cav1.4 KO
-30 mV
-90 mV
f
I/Imax
WT
G369i KI
Cav1.4 KO
Vm (mV)
g
P1
P2
-30 mV
-100 mV
-60 mV
25 mV
100 ms
WT
G369i KI
5 pA
10 ms
P1
P2
h
ns
*
ICa(pA)
P1
P2
P1
P2
WT
G369i KI
i
*
P2/P1
WT
G369i KI

Figure 3

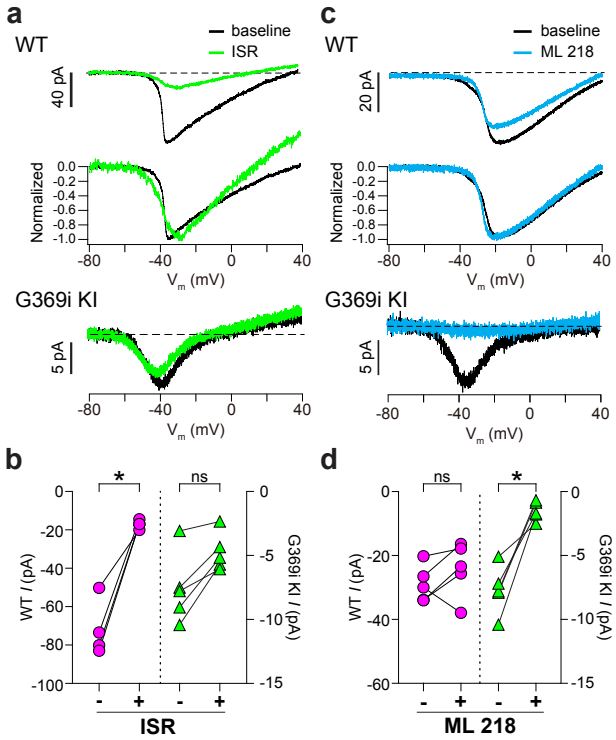
a
WT
baseline
ISR
40 pA
Normalized
0.0
-0.2
-0.4
-0.6
-0.8
-1.0
-80
-40
0
40
V_m (mV)
G369i KI
5 pA
c
WT
baseline
ML 218
20 pA
G369i KI
5 pA
b
*
ns
WT I (pA)
G369i KI I (pA)
ISR
d
ns
*
ML 218

Figure 4

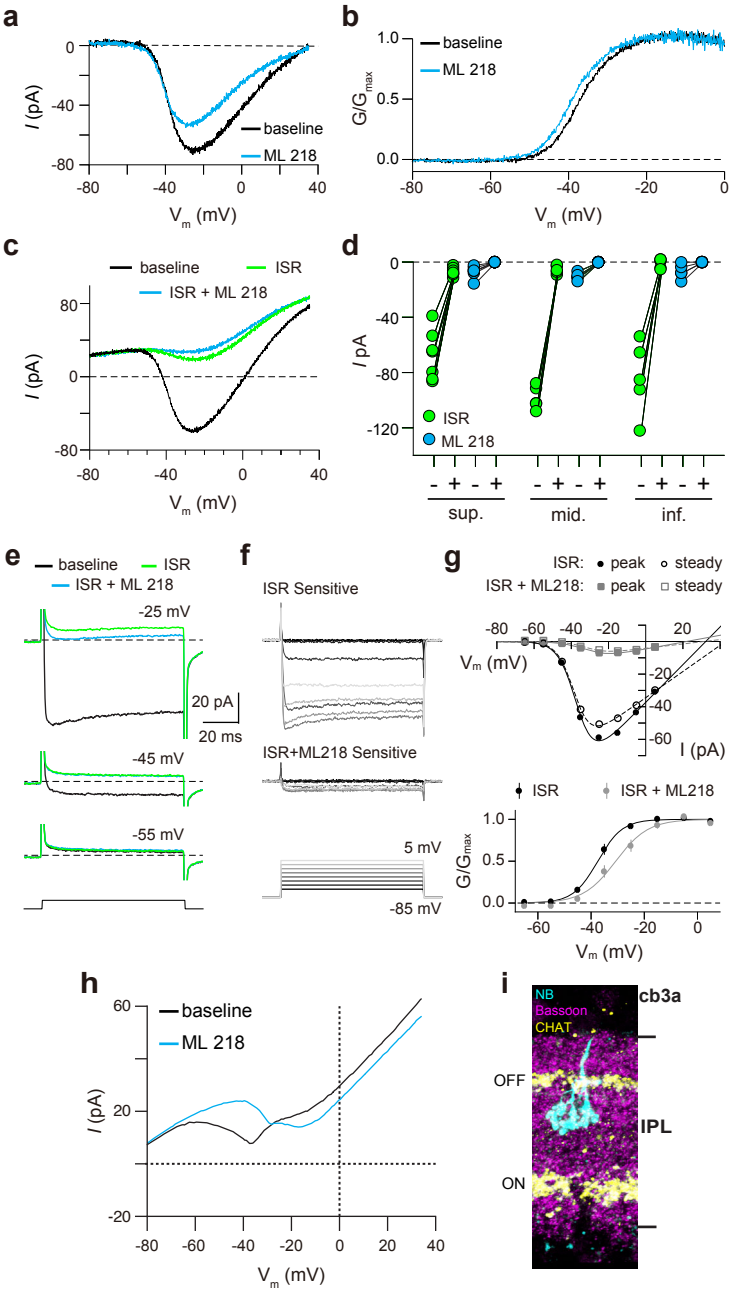
a
I (pA)
baseline
ML 218
V_m (mV)
b
G/G_max
baseline
ML 218
V_m (mV)
c
baseline
ISR
ISR + ML 218
I (pA)
V_m (mV)
d
I pA
ISR
ML 218
sup.
mid.
inf.
e
baseline
ISR
ISR + ML 218
-25 mV
20 pA
20 ms
-45 mV
-55 mV
f
ISR Sensitive
ISR+ML218 Sensitive
5 mV
-85 mV
g
ISR: peak steady
ISR + ML218: peak steady
V_m (mV)
I (pA)
ISR
ISR + ML218
G/G_max
V_m (mV)
h
baseline
ML 218
I (pA)
V_m (mV)
i
NB
Bassoon
CHAT
cb3a
OFF
IPL
ON

Figure 5

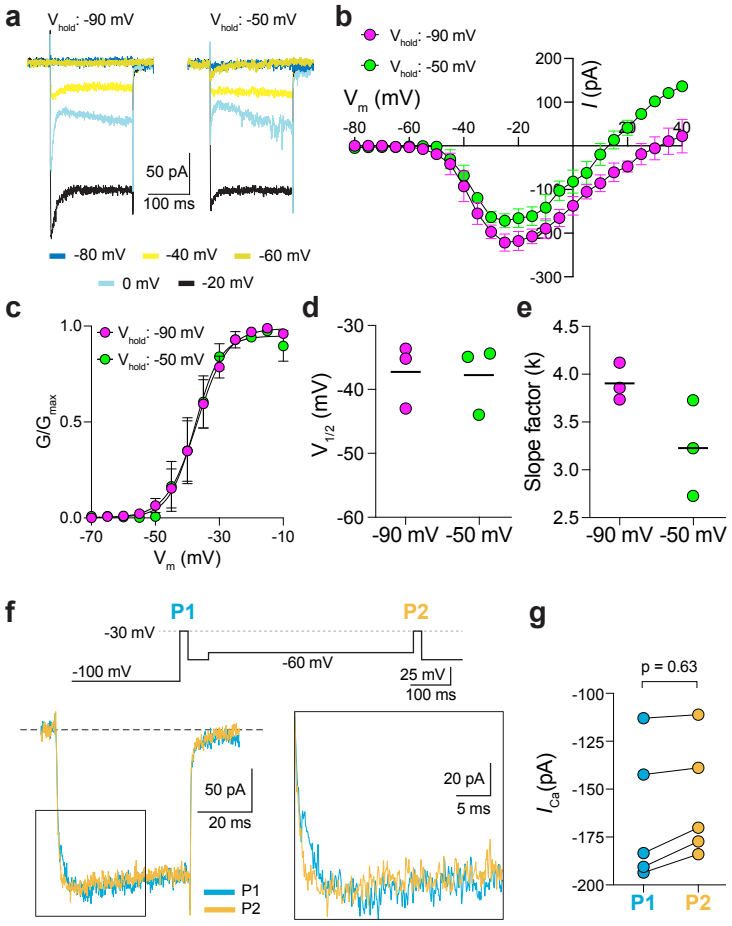
a
V hold: -90 mV
V hold: -50 mV
50 pA
100 ms
-80 mV
-40 mV
-60 mV
0 mV
-20 mV
b
V hold: -90 mV
V hold: -50 mV
V m (mV)
I (pA)
c
G/G max
V m (mV)
d
V 1/2 (mV)
-90 mV -50 mV
e
Slope factor (k)
-90 mV -50 mV
f
P1
P2
-30 mV
-100 mV
-60 mV
25 mV
100 ms
50 pA
20 ms
20 pA
5 ms
g
p = 0.63
I Ca (pA)
P1
P2

Figure 6

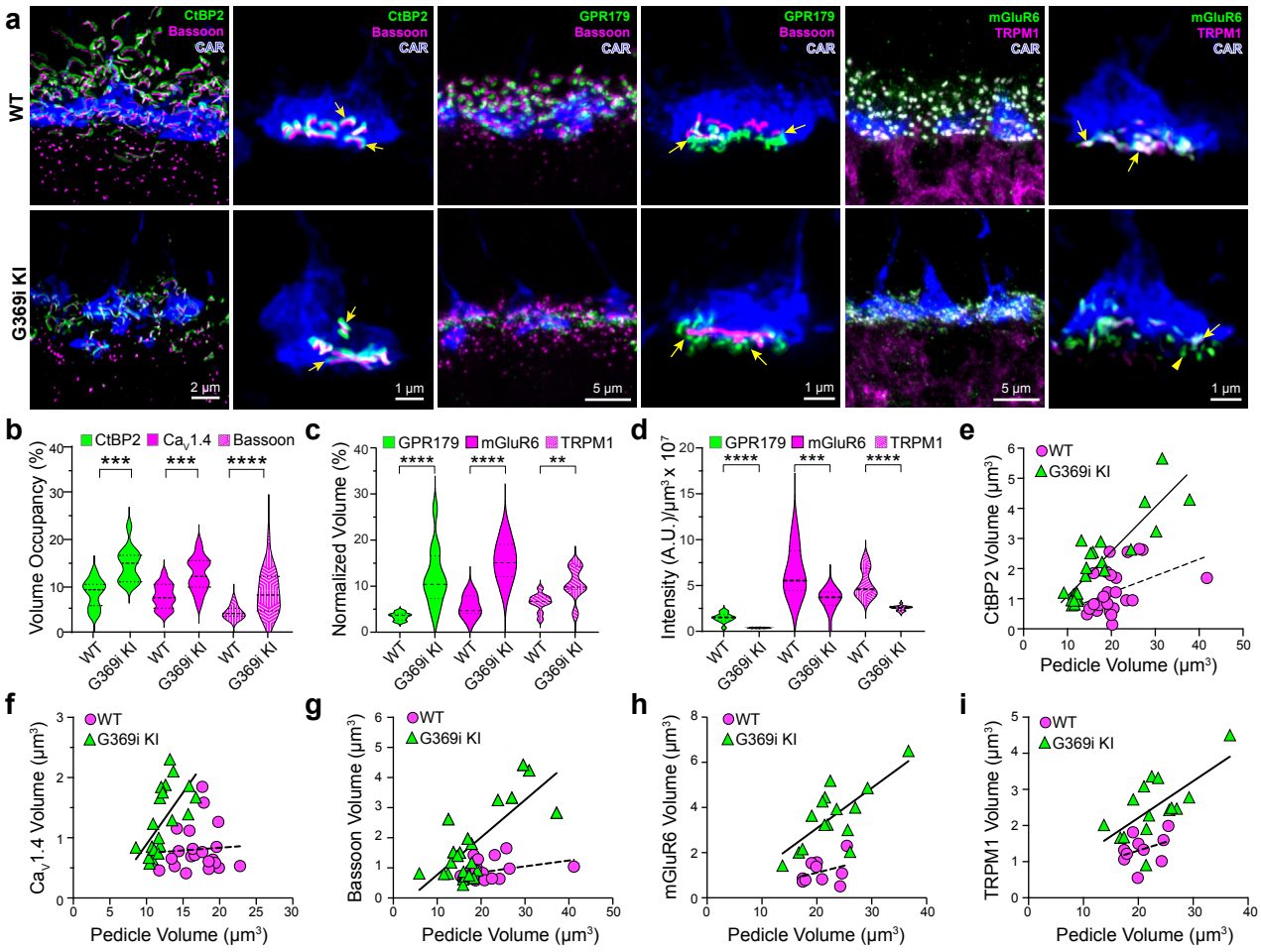
a
WT
G369i KI
CtBP2
Bassoon
CAR
GPR179
mGluR6
TRPM1
2 µm
1 µm
5 µm
b
CtBP2
Cav1.4
Bassoon
Volume Occupancy (%)
c
GPR179
mGluR6
TRPM1
Normalized Volume (%)
d
Intensity (A.U.)/µm³ x 10⁷
e
WT
G369i KI
CtBP2 Volume (µm³)
Pedicle Volume (µm³)
f
Cav1.4 Volume (µm³)
g
Bassoon Volume (µm³)
h
mGluR6 Volume (µm³)
i
TRPM1 Volume (µm³)

Figure 7

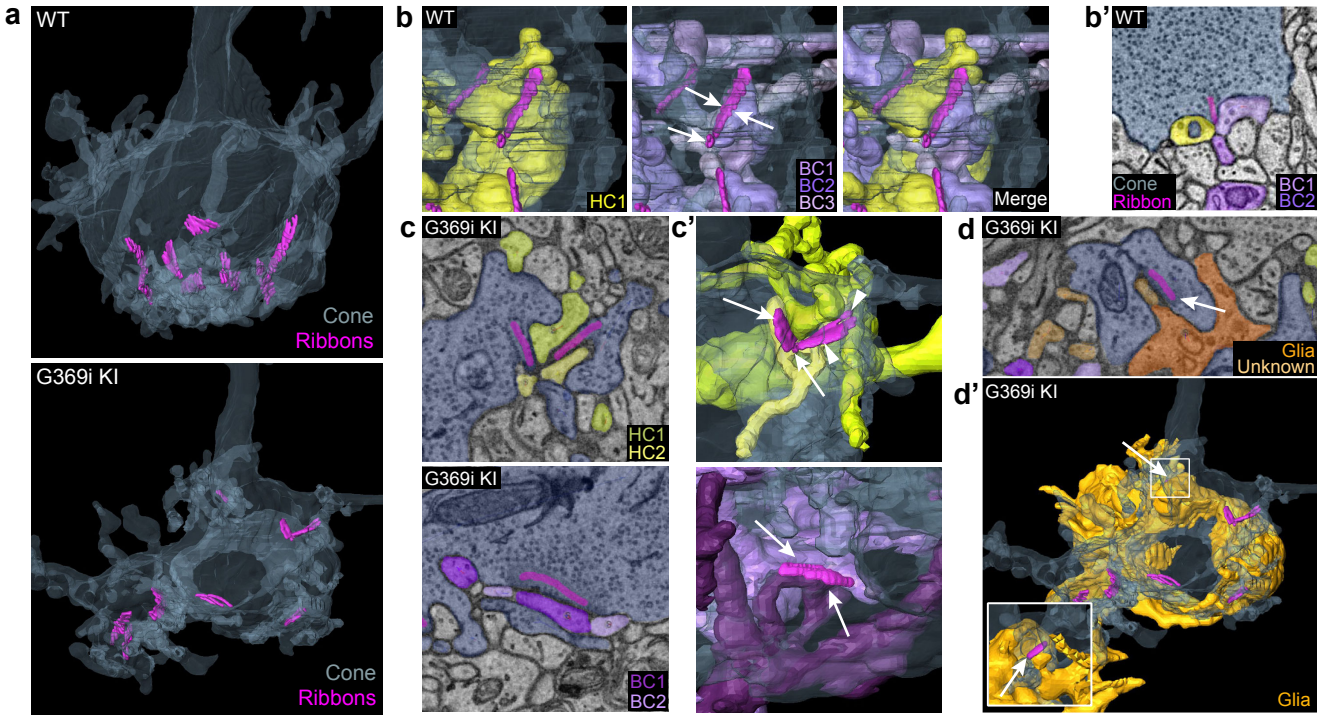
a
WT
Cone
Ribbons
G369i KI
Cone
Ribbons
b
WT
HC1
BC1
BC2
BC3
Merge
b'
WT
Cone
Ribbon
BC1
BC2
c
G369i KI
HC1
HC2
G369i KI
BC1
BC2
c'
d
G369i KI
Glia
Unknown
d'
G369i KI
Glia

Figure 8

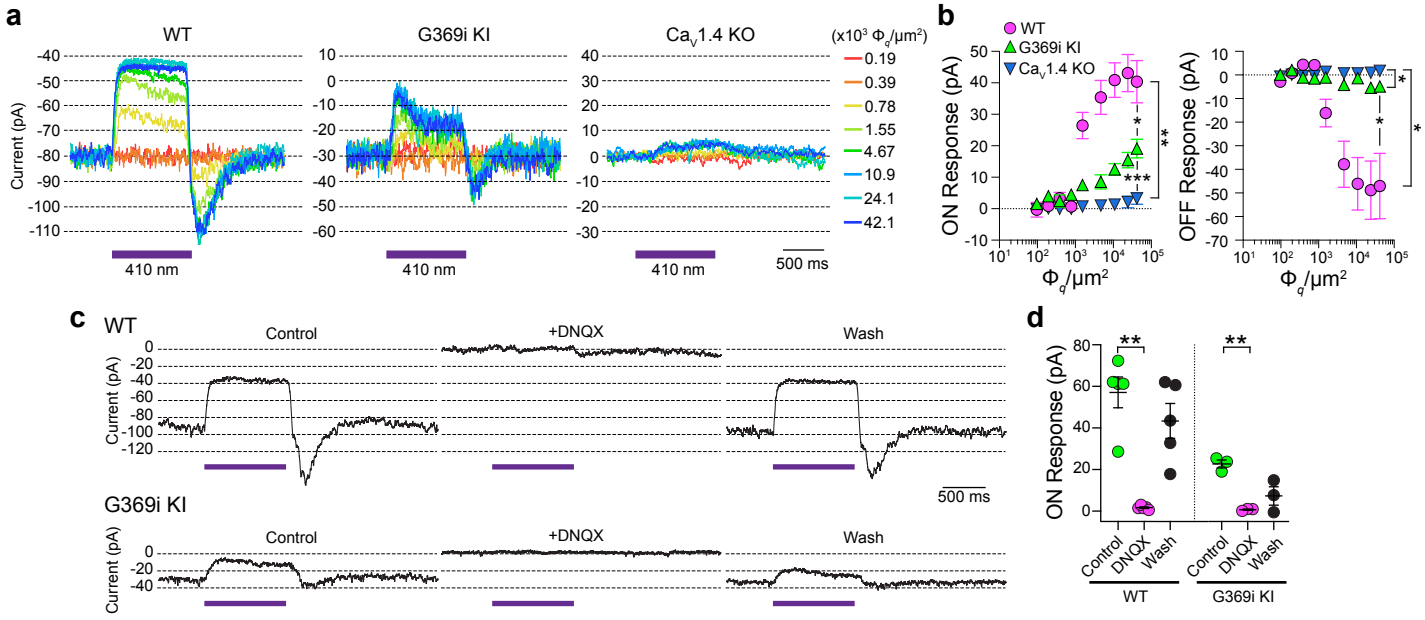
a
WT
G369i KI
Ca$_V$1.4 KO
(x10^3 Φ$_q$/μm^2)
0.19
0.39
0.78
1.55
4.67
10.9
24.1
42.1
Current (pA)
410 nm
500 ms
b
WT
G369i KI
Ca$_V$1.4 KO
ON Response (pA)
OFF Response (pA)
Φ$_q$/μm^2
c
WT
Control
+DNQX
Wash
Current (pA)
500 ms
G369i KI
d
ON Response (pA)
Control
DNQX
Wash
WT
G369i KI

Figure 9

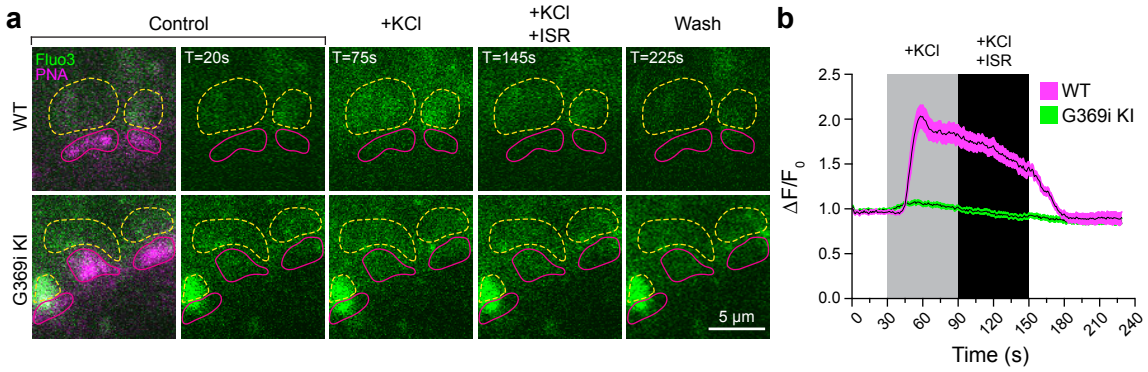
a
Control
+KCl
+KCl
+ISR
Wash
Fluo3
PNA
T=20s
T=75s
T=145s
T=225s
WT
G369i KI
5 µm
b
+KCl
+KCl
+ISR
WT
G369i KI
ΔF/F0
2.5
2.0
1.5
1.0
0.5
0.0
0
30
60
90
120
150
180
210
240
Time (s)

Figure 10

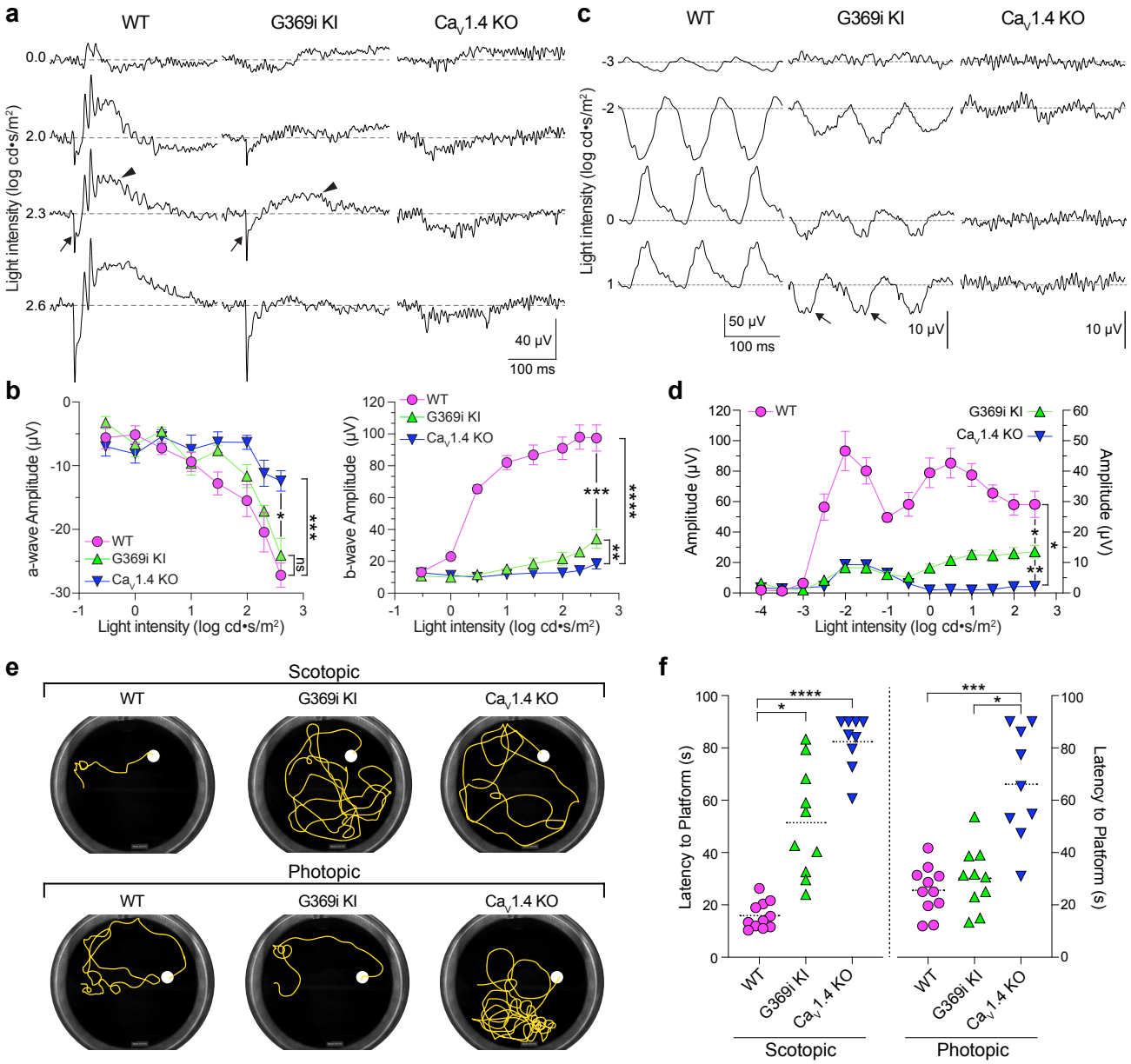
a
WT
G369i KI
Ca$_V$1.4 KO
Light intensity (log cd•s/m²)
0.0
2.0
2.3
2.6
40 µV
100 ms
c
WT
G369i KI
Ca$_V$1.4 KO
Light intensity (log cd•s/m²)
-3
-2
0
1
50 µV
100 ms
10 µV
10 µV
b
a-wave Amplitude (µV)
WT
G369i KI
Ca$_V$1.4 KO
Light intensity (log cd•s/m²)
ns
b-wave Amplitude (µV)
Light intensity (log cd•s/m²)
d
Amplitude (µV)
Light intensity (log cd•s/m²)
e
Scotopic
WT
G369i KI
Ca$_V$1.4 KO
Photopic
WT
G369i KI
Ca$_V$1.4 KO
f
Latency to Platform (s)
WT
G369i KI
Ca$_V$1.4 KO
Scotopic
Photopic

Supplementary Table 1. Statistical analysis of visible platform swim test disaggregated by sex

Male versus Female WT (Photopic)	SS	DF	MS	F (DFn, DFd)	P value
Trial x Genotype	1125	5	224.9	F (5, 45) = 0.6060	P=0.6956
Trial	3564	5	712.9	F (5, 45) = 1.921	P=0.1096
Genotype	273.6	1	273.6	F (1, 9) = 0.6616	P=0.4370
Subject	3722	9	413.5	F (9, 45) = 1.114	P=0.3727
Residual	16703	45	371.2		
Male versus Female G369i KI (Photopic)	SS	DF	MS	F (DFn, DFd)	P value
Trial x Genotype	1457	5	291.4	F (5, 45) = 0.5362	P=0.7477
Trial	3516	5	703.2	F (5, 45) = 1.294	P=0.2833
Genotype	1150	1	1150	F (1, 9) = 0.8168	P=0.3897
Subject	12675	9	1408	F (9, 45) = 2.592	P=0.0168
Residual	24451	45	543.4		
Male versus Female Cav1.4 KO (Photopic)	SS	DF	MS	F (DFn, DFd)	P value
Trial x Genotype	1736	5	347.1	F (5, 35) = 0.6597	P=0.6563
Trial	993	5	198.6	F (3.056, 21.39) = 0.3775	P=0.7737
Genotype	78.37	1	78.37	F (1, 7) = 0.03788	P=0.8512
Subject	14481	7	2069	F (7, 35) = 3.932	P=0.0029
Residual	18416	35	526.2		
Male versus Female WT (Scotopic)	SS	DF	MS	F (DFn, DFd)	P value
Trial x Genotype	862	5	172.4	F (5, 45) = 0.6907	P=0.6331
Trial	914.5	5	182.9	F (5, 45) = 0.7328	P=0.6027
Genotype	634.7	1	634.7	F (1, 9) = 2.121	P=0.1793
Subject	2693	9	299.3	F (9, 45) = 1.199	P=0.3193
Residual	11232	45	249.6		
Male versus Female G369i KI (Scotopic)	SS	DF	MS	F (DFn, DFd)	P value
Trial x Genotype	7648	5	1530	F (5, 45) = 2.581	P=0.0390
Trial	1644	5	328.8	F (5, 45) = 0.5547	P=0.7339
Genotype	4712	1	4712	F (1, 9) = 4.716	P=0.0580
Subject	8993	9	999.2	F (9, 45) = 1.686	P=0.1206
Residual	26671	45	592.7		
Male versus Female Cav1.4 KO (Scotopic)	SS	DF	MS	F (DFn, DFd)	P value
Trial x Genotype	1727	5	345.4	F (5, 35) = 1.470	P=0.2246
Trial	12215	5	2443	F (2.802, 19.62) = 10.40	P=0.0003
Genotype	96.33	1	96.33	F (1, 7) = 0.1346	P=0.7246
Subject	5011	7	715.9	F (7, 35) = 3.046	P=0.0131
Residual	8225	35	235		

Data were analyzed by two-way repeated measures ANOVA. SS, sums of squares; DF, degrees of freedom; MS, mean square; F(DFn, DFd), F statistic.

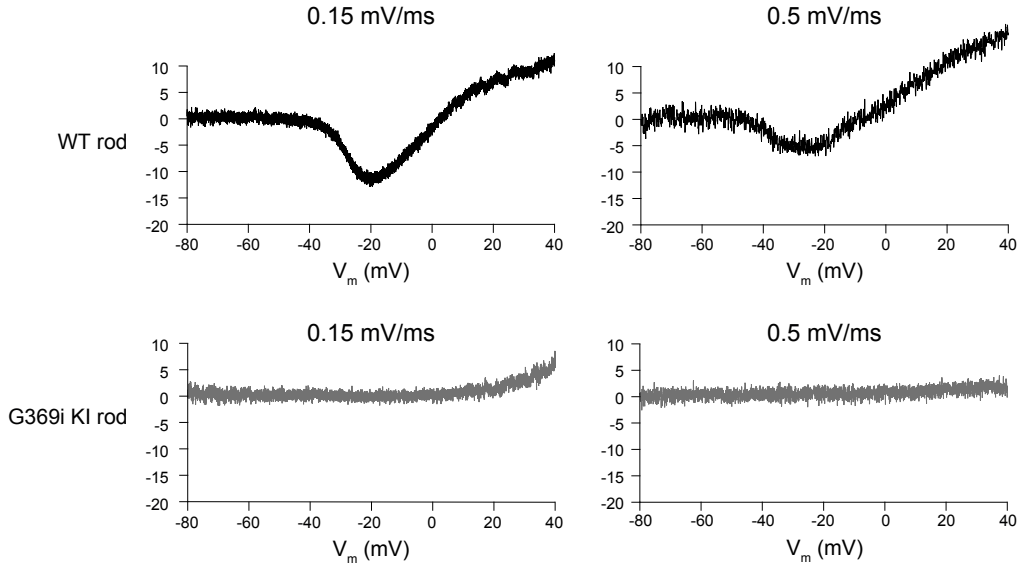

Supplementary Figure S1. Voltage ramps do not reveal I_{Ca} in rods of G369i KI mice. I_{Ca} was evoked by voltage ramps at 0.15 mV/ms or 0.5 mV/ms in rods of WT or G369i KI mice.

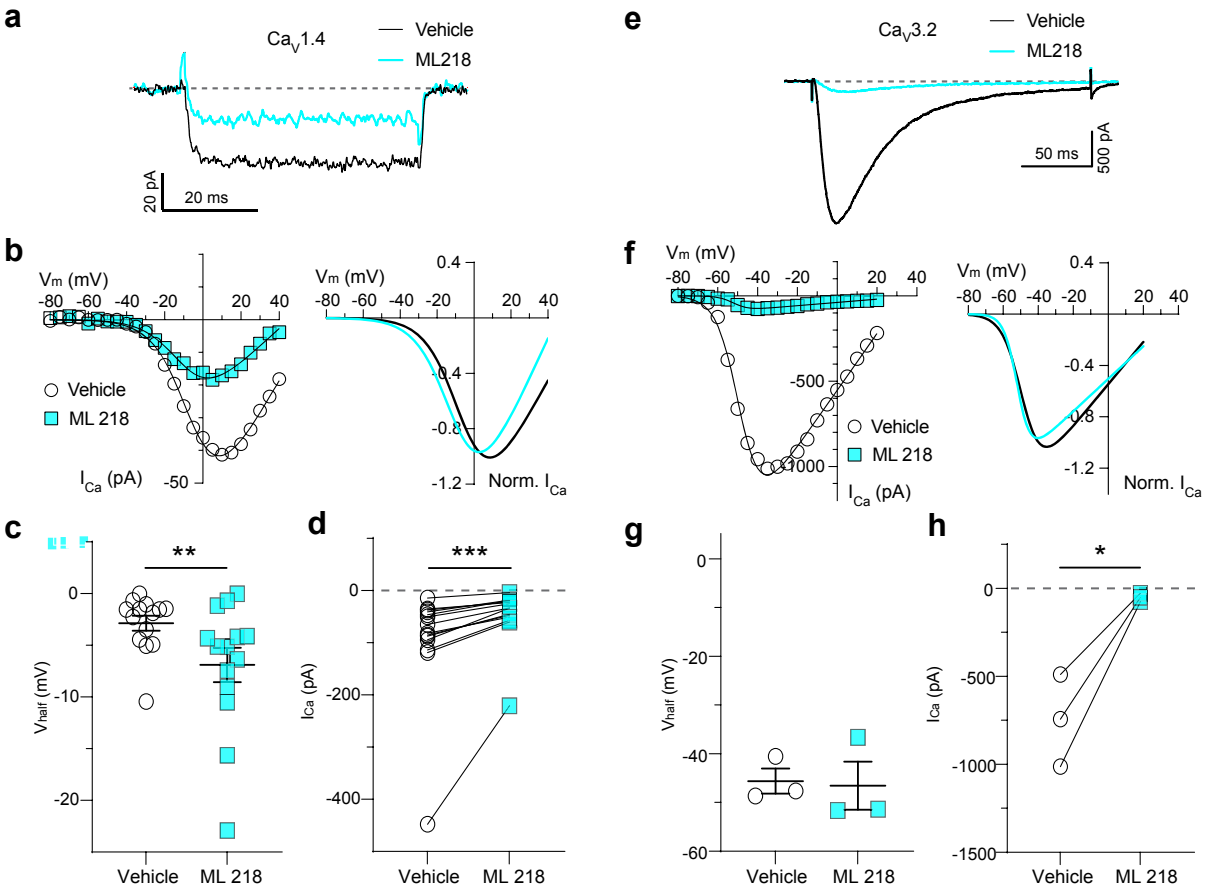

Supplementary Figure S2. Effect of 218 on Ca$_v$1.4 and Ca$_v$3.2 in EK293T cells. Cells were transfected with Ca$_v$1.4, 2x13, and 2 4 (a d) or Ca$_v$3.2 (e h). ***a,e***, epresentative traces and I V plots for I_{Ca} evoked by 50 ms steps to 10 mV (a) or 200 ms steps to 35 mV (e) from a holding voltage of 90 mV. Currents were recorded in the presence of vehicle (SO) or 218 (5 for Ca$_V$1.4 and 1 for Ca$_V$3.2). ***b,f***, eft, I V relationships for data obtained as in *a,e* but using steps to various voltages from a single representative cell. ight, olt mann fit of the responses, normali ed to the maximum I_{Ca} amplitude. ***c,d,g,h***, Graphs depicting effect of 218 on Vhalf (c,g) and I_{Ca}. ** W= 93.00, = 3.1366, p=0.001 *** W=105.0, =3.8419, p=0.0001 both by Wilcoxon matched pairs signed rank test. * t(2)=0.582, p=0.0366 by paired t test.

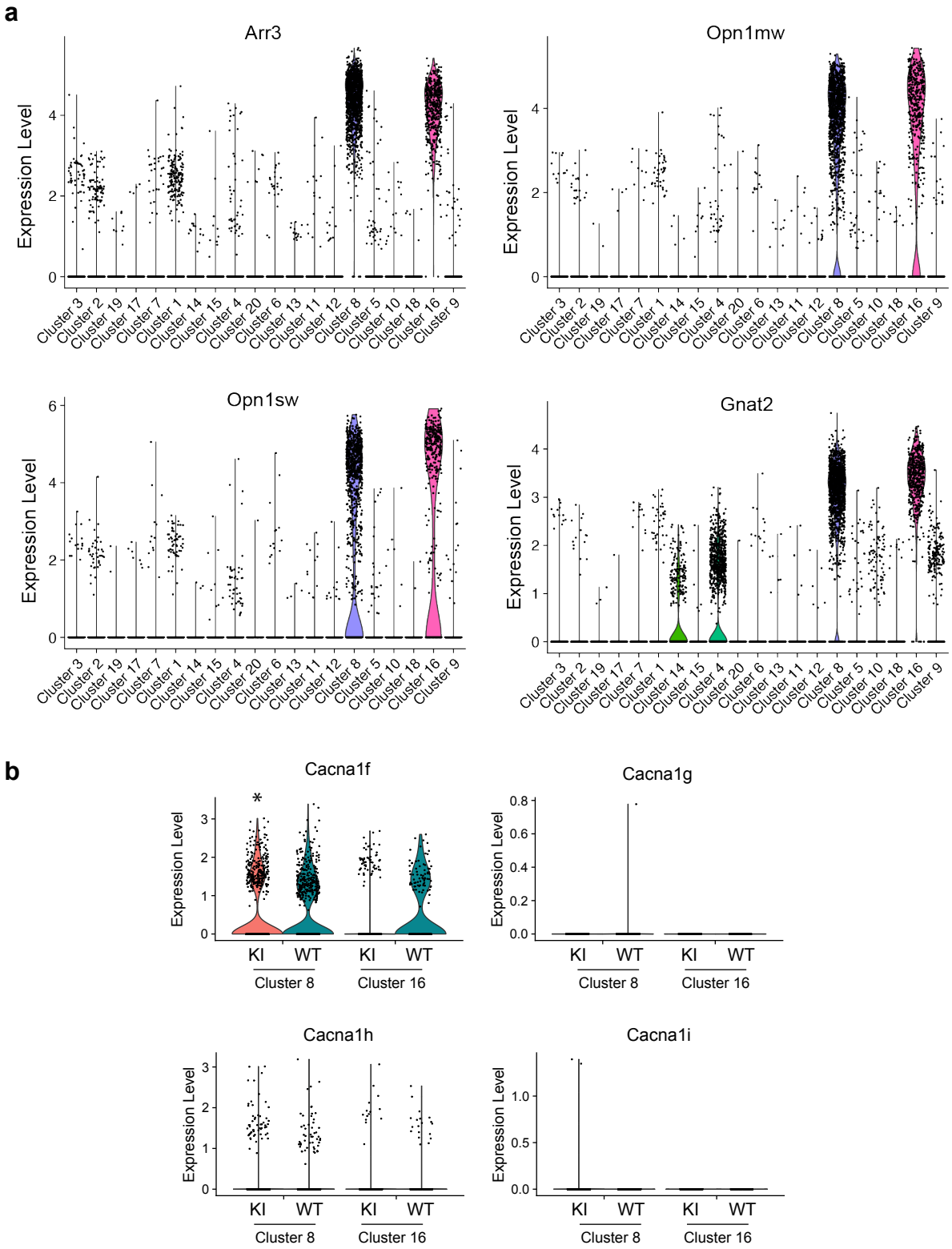

Supplementary Figure S3. Violin plots showing expression levels of transcripts at the single cell level in the retina of WT and G369i KI mice. Each point represents result from a single cell. ***a***, Expression levels of transcripts known to be expressed in cones. Cells were grouped according to their transcriptional profiles using unsupervised clustering. Clusters 8 and 16 were identified as cones based on their high expression of Arr3, Opn1mw, Opn1sw, and Gnat2. ***b***, Expression of transcripts that encode Cav1.4 (Cacna1f) and Cav3 subtypes (Cacna1g, Cacna1h, Cacna1i) in clusters 8 and 16 in retina from WT and G369i KI mice. In cluster 8, there was a small but significant decrease in the level of Cacna1f in the G369i KI vs WT (*, $p = 0.01$) but not in cluster 16 ($p = 0.09$). There was no significant difference in the level of Cacna1h between genotypes in cluster 8 or 16 ($p = 1$).